AFRL-RY-WP-TR-2017-0219

THERMAL TRANSPORT IN DIAMOND FILMS FOR ELECTRONICS THERMAL MANAGEMENT

Samuel Graham

Georgia Institute of Technology

MARCH 2018
Final Report

STINFO COPY

AIR FORCE RESEARCH LABORATORY
SENSORS DIRECTORATE
WRIGHT-PATTERSON AIR FORCE BASE, OH 45433-7320
AIR FORCE MATERIEL COMMAND
UNITED STATES AIR FORCE

NOTICE AND SIGNATURE PAGE

This report is the result of contracted fundamental research deemed exempt from public affairs security and policy review in accordance with SAF/AQR memorandum dated 10 Dec 08 and AFRL/CA policy clarification memorandum dated 16 Jan 09. This report is available to the general public, including foreign nationals.

Copies may be obtained from the Defense Technical Information Center (DTIC) (http://www.dtic.mil).

AFRL-RY-WP-TR-2017-0219 HAS BEEN REVIEWED AND IS APPROVED FOR PUBLICATION IN ACCORDANCE WITH ASSIGNED DISTRIBUTION STATEMENT.

// Signature//

JOHN D. BLEVINS, Program Manager
Devices for Sensing Branch
Aerospace Components & Subsystems Division

// Signature//

ROSS W. DETTMER, Chief
Devices for Sensing Branch
Aerospace Components & Subsystems Division

// Signature//

JAMES M. SATTLER, Lt Col, USAF
Deputy
Aerospace Components & Subsystems Division
Sensors Directorate

1. REPORT DATE *(DD-MM-YY)*	2. REPORT TYPE	3. DATES COVERED *(From - To)*
March 2018	Final	5 December 2014 – 30 September 2017

4. TITLE AND SUBTITLE	5a. CONTRACT NUMBER
THERMAL TRANSPORT IN DIAMOND FILMS FOR ELECTRONICS THERMAL MANAGEMENT	FA8650-15-C-7517
	5b. GRANT NUMBER
	5c. PROGRAM ELEMENT NUMBER 61101E

6. AUTHOR(S)	5d. PROJECT NUMBER
Samuel Graham	1000
	5e. TASK NUMBER N/A
	5f. WORK UNIT NUMBER Y17C

7. PERFORMING ORGANIZATION NAME(S) AND ADDRESS(ES)	8. PERFORMING ORGANIZATION REPORT NUMBER
Georgia Institute of Technology 771 Ferst Dr Atlanta, GA 30332-0405	

9. SPONSORING/MONITORING AGENCY NAME(S) AND ADDRESS(ES)		10. SPONSORING/MONITORING AGENCY ACRONYM(S)
Air Force Research Laboratory Sensors Directorate Wright-Patterson Air Force Base, OH 45433-7320 Air Force Materiel Command United States Air Force	Defense Advanced Research Projects Agency DARPA/MTO 675 North Randolph Street Arlington, VA 22203	AFRL/RYDD
		11. SPONSORING/MONITORING AGENCY REPORT NUMBER(S) AFRL-RY-WP-TR-2017-0219

12. DISTRIBUTION/AVAILABILITY STATEMENT
Approved for public release; distribution is unlimited.

13. SUPPLEMENTARY NOTES

14. ABSTRACT

This report covers methods to characterize the thermal conductivity and structure of chemical vapor deposition (CVD) diamond grown on gallium nitride (GaN) and silicon (Si). Best practices for determining the thermal conductivity within the first few microns are reported. Finally, methods are characterized which lead to improving the thermal conductivity of CVD diamond and its integration with Si and GaN.

15. SUBJECT TERMS

chemical vapor deposition diamond, thermal conductivity, interface thermal resistance, GaN-diamond integration

16. SECURITY CLASSIFICATION OF:			17. LIMITATION OF ABSTRACT:	18. NUMBER OF PAGES	19a. NAME OF RESPONSIBLE PERSON (Monitor)
a. REPORT Unclassified	**b. ABSTRACT** Unclassified	**c. THIS PAGE** Unclassified	SAR	68	John Blevins **19b. TELEPHONE NUMBER** *(Include Area Code)* N/A

Table of Contents

Section	**Page**

List of Figures

List of Tables

1. Summary

This report chronicles the work completed during the DARPA Diamond Round Robin program with a focus on the final reporting period of the program. The purpose of the program was twofold. First, we focused on the merits of measurement techniques for measuring the thermal conductivity of thin chemical vapor deposited (CVD) diamond films and the thermal boundary resistance with its growth substrate. Second, we focused on understanding the parameters which contributed to the variation in thermal conductivity of CVD diamond films. Through these efforts, we were able to demonstrate the ability to measure the in-plane thermal conductivity of CVD diamond thin films by both local, transient methods (time domain thermal reflectance or TDTR) as well as steady-state techniques (Raman) as originally proposed in the program. To facilitate this comparison between the techniques, a third technique was employed to provide additional and ideally independent validation of the measurements made with the two core metrology methods. For the purposes of comparing the techniques, a small subset of CVD diamond samples fabricated as part of the program were selected. These samples were deposited via identical depositions conditions but employed different sized diamond seeds which lead to differences in crystal growth morphology. These differences in morphology provided a well-controlled, independent variable to be characterized via the three separate thermal metrology techniques.

After establishing the merits of the methods for measuring thermal conductivity, two separate studies focused on the impact of both chemical composition and interfacial patterning on the thermal boundary resistance (TBR) at a material heterointerface containing diamond was conducted. The former study focused on the impact of thin dielectric layers (SiN, AlN, both ~ 5 nm thick) on the thermal boundary resistance at the GaN/CVD diamond interface, ultimately determining that SiN results in the lowest TBR due to a largely defect-free interfacial region with a smooth compositional transition between the GaN and CVD diamond layers. The latter study characterized the influence of geometric patterning on the TBR at Si/CVD diamond heterointerfaces, ultimately showing that the TBR can be lowered compared to a non-patterned, flat heterointerface. Further details related to all these research areas can be found in the subsequent sections of this report.

2. Comparisons of Thermal Metrology Methods for Diamond Thin Film Characterization

A significant component of this program was the round-robin comparison of various thermal metrology techniques for characterizing the thermal conductivity of thin film CVD diamond. The techniques compared were Raman TDTR due to its use in measuring thermal conductivity of thin CVD diamond films in the past. To aid in this comparison, electrical resistance thermometry (ERT) was used as a third technique to help understand any differences between TDTR and Raman. Moreover, the sample designs for the Raman samples were amenable to ERT measurements, and thus, no new samples had to be prepared for this measurement. The aim of this was to better understand the variability and performance of the thermal metrology techniques, evaluating their relative merits and detriments. For comparison purposes, a small subset of the samples fabricated over the duration of the program was selected for these efforts and tested by multiple techniques and by all groups in the program. Materials characterization was also performed on the samples to ensure that the proper physical dimensions were used in the data reduction for thermophysical properties. The diamond was grown by chemical vapor deposition onto 75 mm diameter Si wafers which were then patterned into samples for characterization as shown in Figure 1. These samples included samples designed for TDTR, Raman/ERT, and a common sample that had both test structures included in order to have close physical proximity of the two different measurements.
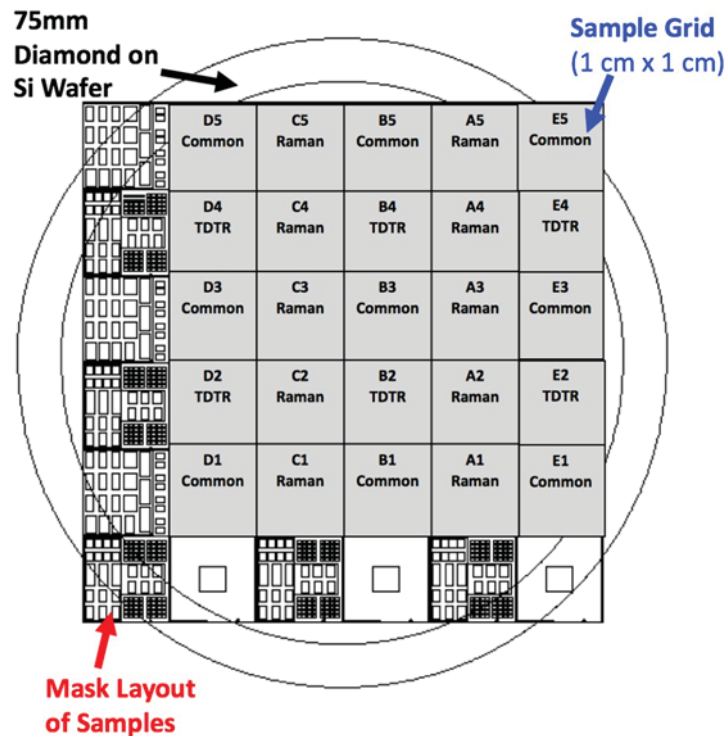
Figure 1: Sample Layout

Depiction of the standard layout of samples on 75 mm diamond on Si wafers. The image shows the wafer with the overlay of the mask layout of the samples and the grid showing the 1 cm x 1 cm samples (TDTR, Raman, or Common) and where they exist on a typical wafer

The focus of this portion of the study to test the accuracy of the three methods was to concentrate on common samples extracted from the wafer in Figure 1. As mentioned, the common sample contained both Raman and TDTR samples in close proximity on the same die. On the die, as shown in Figure 2, there were two Raman samples and two TDTR samples. In order to isolate the in-plane thermal conductivity of the thin diamond films and provide a common structure that can be tested with the various measurement techniques, suspended diamond membranes were fabricated for both the TDTR and Raman samples to force the heat conduction laterally. Figure 3 shows a cross-sectional diagram of the membrane structure, illustrating its ability to provide a platform where three different measurement techniques can be applied.
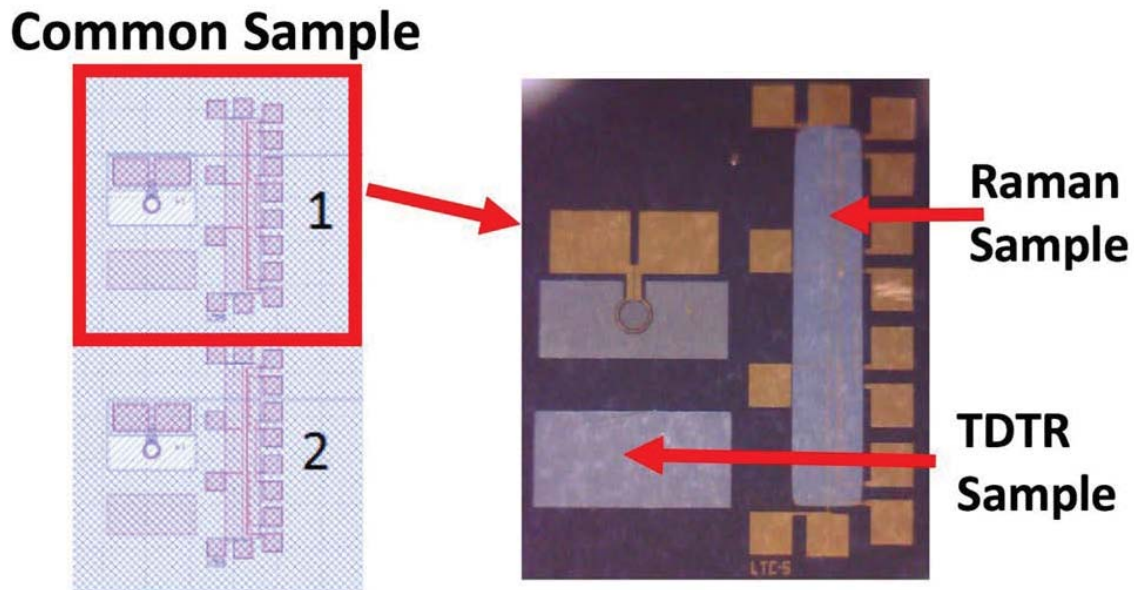
Figure 2: Description of Common Sample
Image showing the layout of the common sample used for measuring thermal conductivity and comparing Raman, TDTR, and ERT techniques. There are two identical samples on each die with the upper Raman and TDTR membranes labeled 1 and the lower Raman and TDTR membranes labeled as 2. The Raman samples were also used for ERT measurements.

Two of the three methods used to characterize the in-plane thermal conductivity of the membranes are steady-state techniques that measure the temperature profile from the central heater out to the supported areas at the edges. Raman thermometry and ERT provide separate methods to characterize the temperature gradient via optical and electrical thermometry, respectively. The separate data sets collected via both technique can then be fit with a common finite element model (FEM) to extract the thermal conductivity, providing a means to evaluate any potential differences in the raw data generated by the methods. Finally, the TDTR measurements provide a non-contact, transient thermal characterization technique with both the temporal and spatial resolution to provide insight regarding local phonon transport processes which can then be compared to the results from the steady-state methods.
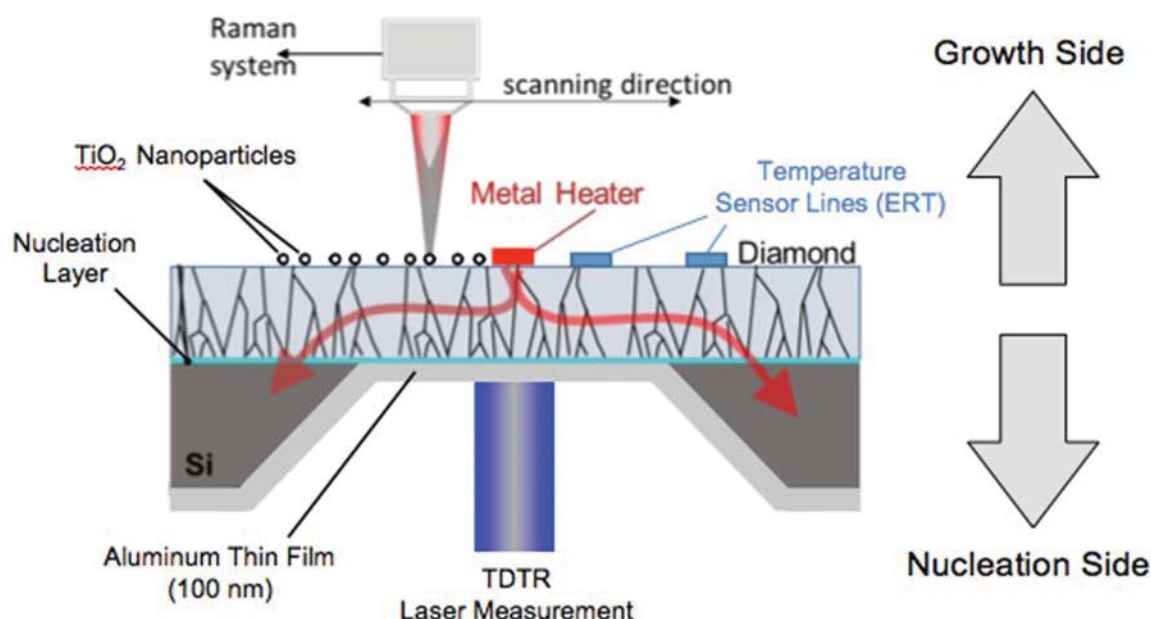
Figure 3: Membrane Sample for Lateral Thermal Conductivity Measurements
Cross-section diagram of the thin film CVD diamond membrane structures used in this study to perform the in-plane thermal conductivity measurements. Steady-state measurements performed via Raman thermometry and electrical resistance thermometry (ERT) were performed on the growth side of the membrane, while TDTR measurements were performed on the nucleation side

2.1 Sample Preparation

The nanocrystalline diamond (NCD) suspended membrane samples examined for this effort were polycrystalline films grown by CVD on 200 μm thick Si wafers. Sample A (NRL 010516; Die A5) was grown from 4 nm seeds at a growth temperature of 750°C and with a plasma power of 2200 W and contains two membranes, M1 (upper) and M2 (lower) as seen in Figure 2, designed to accommodate Raman and ERT measurements for determination of the NCD in-plane (lateral) thermal conductivity [see Figure 4(a)]. Sample B (NRL 122315; Die E3) was grown from 40 nm seeds at a growth temperature of 750°C and with a plasma power of 2300 W and contains two membranes, M1 and M2, designed to accommodate Raman and ERT measurements [see Figure 4(b)]. It should be noted that all test samples (Raman, TDTR, and ERT) were placed on the same die next to each other to minimize the impact of diamond property variation across a wafer which could contribute to variations between the measurement techniques. By limiting the measurements to the same local region, it was assumed that the variations observed between the methods arise from intrinsic characteristics or errors from the methods.

To supply a measureable and controllable heat source to the diamond films, metal line structures were fabricated by depositing a 5 μm-wide and 10 nm-thick adhesion layer of titanium (Ti) followed by 200 nm of gold (Au) by the Naval Research Laboratory. To confine the input heat flow to the lateral (in-plane) directions, suspended membranes were constructed by etching away a 2000 x 400 μm area of Si substrate beneath the diamond film. To facilitate the TDTR measurements on these sample membranes, 100 nm of aluminum was evaporated onto the

"nucleation" side of the diamond thin films that was exposed following the etching of the silicon substrate. The nucleation side of the CVD diamond is preferable for the TDTR measurements due to the fact that the surface roughness of the film is considerably smaller on this side compared to the growth side.

The centerline metal structure was used as a resistive heater to dissipate heat laterally (x-direction) to produce one-dimensional (1D) thermal conduction in the longitudinal (y-direction) center of the membrane and hence a linear temperature profile spanning the membrane width. Negligible (< 0.5%) deviation from 1D conduction was observed near the center of the membrane that is bounded in the y-direction by ±250 µm (hereafter referred to as the 1D regime) [see Figure 4c]. The 5:1 length-to-width aspect ratio of the membranes examined in this study was determined to be ideal for achieving 1D conduction across the 2D NCD membrane by performing parametric analysis via a finite element model (FEM) constructed in ANSYS Design Modeler and Mechanical Applications and used as a theoretical model for the Raman thermometry and ERT techniques. By varying the membrane width for a fixed membrane length of 2000 µm and assessing the membrane in-plane thermal conductivity according to Fourier's law for 1D conduction for each dimensional configuration, it has been observed that a 5:1 length-to-width aspect ratio yields an analytical thermal conductivity most closely matching the "true" thermal conductivity prescribed in the FEM [see Figure 5].

| (a) | (b) | (c) |
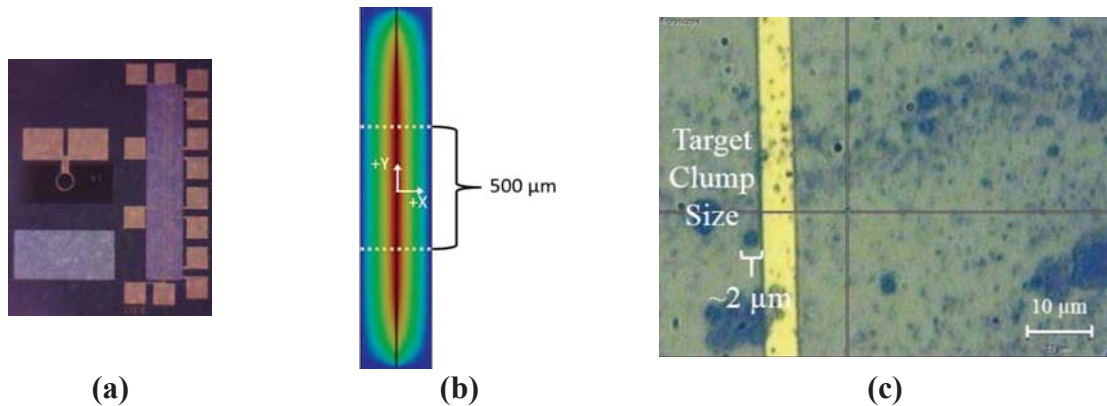
Figure 4: Common Sample for Raman and ERT Measurements

Image of (a) Common Sample A where image shows (right) a membrane structure for Raman thermometry and ERT as also depicted in Figure 2, (bottom left) a membrane structure for TDTR as shown in Figure 2. (b) Surface temperature map of Raman/ERT membrane from FEM modeling depicting 1D heat transfer regime. (c) Optical microscope (100x) image of the surface of a Raman/ERT sample showing the central line heater and surface-deposited TiO_2 particles for Raman measurements
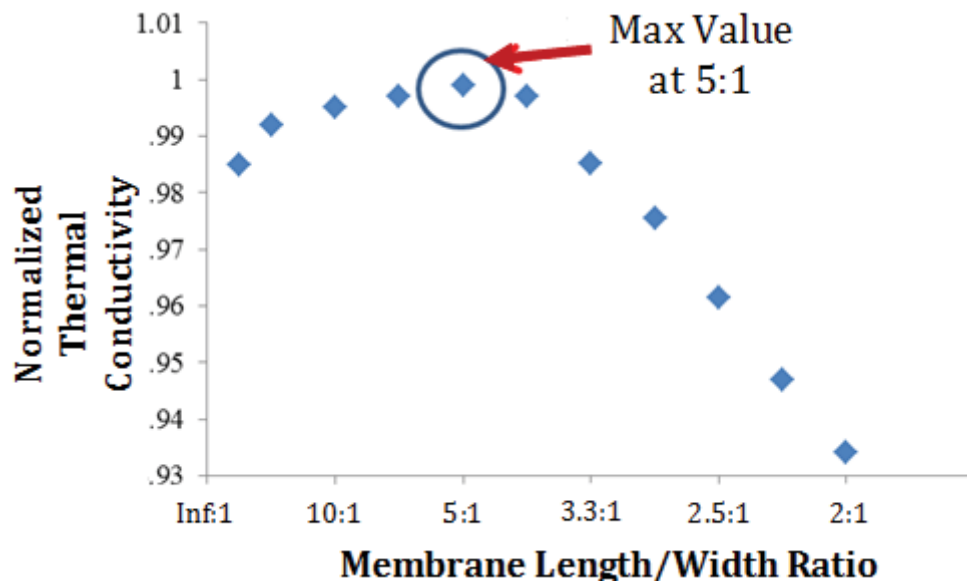
Figure 5: Optimal Membrane Size for Raman and ERT Measurements
FEM calculations showing the impact of membrane length to width ratio on the 1-D heat transfer assumption in the membrane. The data shows the normalized thermal conductivity which is from the calculated thermal conductivity from the finite element analysis (FEA) simulations divided by the known thermal conductivity of the membrane used in the simulation. The calculated thermal conductivity is taken by dividing the heat flux by the temperature gradient across the central width of the sample.

Due to the fact that the stress distribution in the diamond membrane can impact the Raman measurements, Raman active nanoparticles were used as a stress independent thermal sensor on top of the membrane. To accomplish this, TiO_2 nanopowder of 99.9% purity and 32 nm average particle size acquired from Alfa Aesar was suspended in isopropyl alcohol (IPA) and was deposited via drop casting on the NCD membrane samples while heated to 85°C to accelerate solvent evaporation. The nanoparticle aggregates (hereafter referred to as particles for simplicity) present on the membrane surface after deposition were clearly observed when viewed using 100x magnification [see Figure 4(d)]. As illustrated in Figure 4(d), particles measuring between 1-2 µm in diameter were used as local temperature sensors for Raman thermometry. Particles used as temperatures sensors should be as small as possible to optimize the spatial resolution of temperature measurements, however particles smaller than 1 µm in diameter were observed to produce insufficient Raman scattering intensity for resolving distinguished Raman spectrum peaks.

2.2   Raman Thermometry

Raman thermometry, a non-contact, non-destructive, and material-specific thermal characterization technique capable of high thermal and spatial resolutions (~1°C and ~1 µm, respectively), was used to measure the temperature distribution present across the CVD NCD membrane samples when electrical power was supplied to the centerline resistive heater. Based on a comprehensive summary of the methods commonly used to perform Raman thermometry and their respective advantages and disadvantages [1], the peak position method for Raman

Approved for public release; distribution is unlimited.

thermometry was used in the present work due to its experimental practicality. Keithley 2400 Source Meters were used to supply 200 ± 0.2 mW of electrical power and monitor electrical characteristics of the metal centerline heater on the membrane samples via 4-point measurement. The Raman thermometry measurements were conducted using a Renishaw InVia Raman system with a 488 nm Ar+ excitation laser that was focused through a Leica 0.75 N.A. 100x objective to resolve a ~1 µm spot size. The temperature dependence of the measured Raman shift of surface deposited particles was determined by incrementally heating the sample to increasing temperatures using an INSTEC mk1000 temperature controller and thermal stage, and collecting Raman measurements under the steady-state conditions of each temperature step. A peak shift-temperature calibration coefficient, A_ω cm^{-1}/°C, was extracted from the resulting linear peak position-temperature relation:

$$A_\omega = \frac{\omega - \omega_o}{T - T_o} \tag{1}$$

where ω and ω_o are the Raman peak positions measured from the subject material at the incremented and reference condition thermal stage temperatures, respectively, and T and T_o are the incremented and reference condition thermal stage temperatures, respectively, as measured by a Fluke 54IIB Thermometer using a K-type thermocouple (TC) [see Figure 6(a)]. To ensure that peak position-temperature calibrations on TiO_2 particles did not vary from particle to particle, calibrations were performed on particles deposited on several suspended membrane samples. Further, to ensure that calibrations were not subject to a systemic error resulting from measuring particles located on suspended membranes, a calibration was performed on a particle deposited on a GaN/SiC wafer fragment. The results of these calibrations demonstrate precise consistency and are in agreement with literature [2] [see Figure 6(b)]. The mean value of the five measured calibration coefficients was determined to be $0.0252 \pm 4.2 \times 10^{-1}$ cm^{-1}/°C and was used as the nominal value for subsequent thermal analysis.
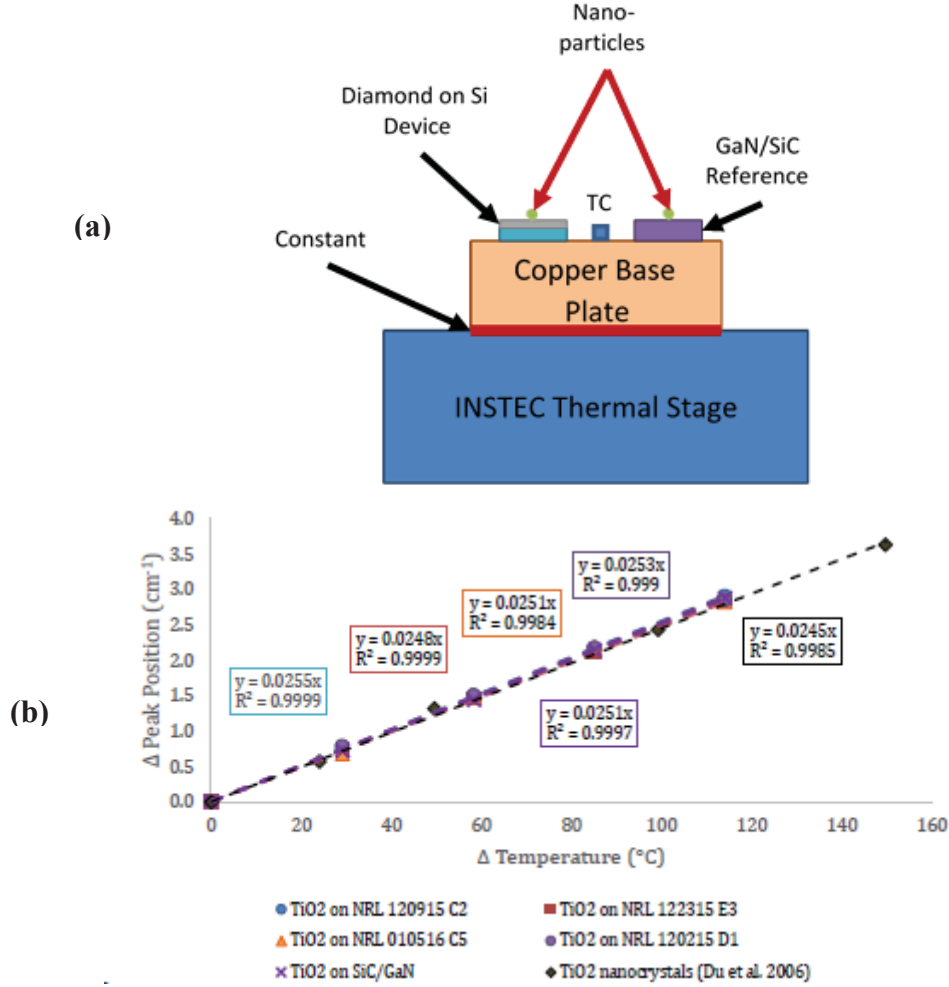
Figure 6: Raman Calibration of Nanoparticles for Temperature Measurements
(a) Schematic of calibration experimental apparatus and (b) measured TiO₂ particle calibration results supported by literature [2].

To experimentally measure the lateral (1D) temperature distribution of the NCD membrane during powered conditions, temperature measurements were sequentially collected across the membrane width via Raman thermometry of surface-deposited TiO₂ particles positioned within the 1D regime while the thermal stage was held at a controlled 30°C isothermal ground condition. Additional Raman thermometry measurements were collected from particles positioned over the Si substrate on either side of the centerline heater to capture the decay of lateral thermal conduction approaching an isothermal condition. A more accurate temperature measurement of the thermal ground condition was obtained by directly probing the top of the Si substrate on both sides of the centerline heater at locations at least 50 μm from the membrane edge. Direct Raman thermometry measurement of the Si substrate was possible because the excitation laser used (488 nm) transmits through the TiO₂ particles and NCD membrane due to their wide band gaps [3, 4], and is absorbed by the Si substrate with a shallow penetration depth of ~0.5 μm [5]. Each Raman thermometry measurement was a result of averaging 20 spectral acquisitions collected before, during, and after the imposed power condition to account for sampling variance. All acquired spectra were fit to a pseudo-Voigt function to extract the

8
Approved for public release; distribution is unlimited.

spectral parameters of interest: peak position, intensity, and full width at half maximum (FWHM). The reference conditions collected before and after each power condition were used to resolve a temperature measurement using the peak position method for Raman thermometry [1] and to ensure measurement conditions were unchanged throughout each measurement.

The lateral thermal conductivity, k_{Raman}, of each sample was deduced from the experimental temperature data, $T_{exp}(p_i)$, by fitting the numerical temperature solutions, $T_{FEM}(p_i)$, of a three-dimensional (3D) steady-state thermal FEM of the full membrane structure and surface-deposited particles, where p_i denotes the ith particle, p, on each sample. The optimal value of k_{Raman} was resolved by identifying the thermal conductivity input to the FEM that minimized the error between $T_{exp}(p_i)$ and $T_{FEM}(p_i)$. The FEM considered convection, radiation, the temperature dependent thermal conductivities of the Si substrate and metal (Au) line structures [6], the effective thermal conductivity of nanoparticle aggregates including particle-particle thermal resistances [7], and the TBRs) between the metal line structures, NCD membrane, Si substrate, and backside Al. All TBRs used for analysis were measured by TDTR according to methods thoroughly explained in literature [8] and are reported in Table 1 as thermal interface conductances (G). It is important to note that the temperature measurements collected from Raman thermometry of particles within a 30 µm lateral proximity of the centerline heater were excluded from the fitting algorithm for resolving k_{Raman} to ensure that measurements were well within the linear temperature distribution predicted by FEM (Figure 7). The exclusion of these centermost temperatures is a reasonable assumption for several reasons. By nature of the temperature calculation according to Equation 1 (where T is now the temperature resolved by Raman thermometry), these peak temperatures are the most uncertain, and there were sufficiently numerous temperature measurements present further from the centerline heater that were observed to precisely match the ideal linear distribution calculated by the FEM.
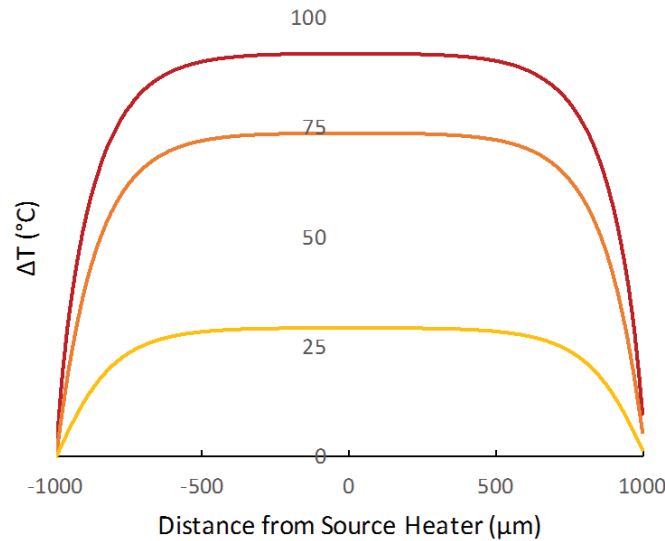
Figure 7: Temperature Distribution across Membrane Width
FEA calculations showing the parabolic temperature profile across the Raman/ERT membrane (5:1 length to width ratio) at different heat powers resulting in different temperature rises. The data show a nearly flat temperature profile in the central portion of the membrane where the 1D temperature assumption is made.

9

2.3   Electrical Resistance Thermometry

ERT was used as a second method for analyzing thermal conductivity as it was amenable to the test structures used for Raman thermal measurements. ERT is performed by measuring the temperature distribution present when electrical power was supplied to the centerline heater by using the heater itself in addition to off-center metal line structures as resistive thermometers or resistance temperature detectors (RTDs) as shown in Figure 8. The off-center RTDs were deposited on the membrane samples such that two independent 4-point measurements could be made at lateral distances of 50 µm (RTD 2) and 150 µm (RTD 3) from the centerline heater, which also functions as an RTD (RTD 1) [see Figure 5]. All of the electrical measurements were collected via 4-point measurements on a Cascade Microtech Summit 11000 probe station using a total of eight needle probes, a Keithley 2400 Sourcemeter to supply electrical power to RTD 1, and an Agilent 34410A 6 ½ Digit Multimeter to sequentially measure the resistances of RTDs 2 and 3. The temperature dependence of the RTD resistances was measured analogously to the surface-deposited TiO2 particles used for Raman thermometry using the same INSTEC mk1000 temperature controller and thermal stage. A calibration coefficient, A_R, was extracted for each metal line structure from the linear relation:

$$A_R = \frac{\frac{R-R_o}{R_o}}{T-T_o} = \frac{\%\Delta R}{\Delta T} \tag{2}$$

where R and R_o are the resistances measured at the incremented and reference condition thermal stage temperatures, respectively, and T and T_o are the incremented and reference condition of the thermal stage temperatures, respectively, as measured by the same Fluke 54IIB Thermometer and K-type TC. However, it is important to note that A_R determined for each RTD was evaluated as a *percent* change in resistance with respect to a change in temperature so that A_R is an intrinsic property assessment independent of the magnitude of resistance measured. Thus, A_R extracted from the 2000 µm long centerline heater and 500 µm long RTDs were assessed to be nearly equivalent in magnitude.
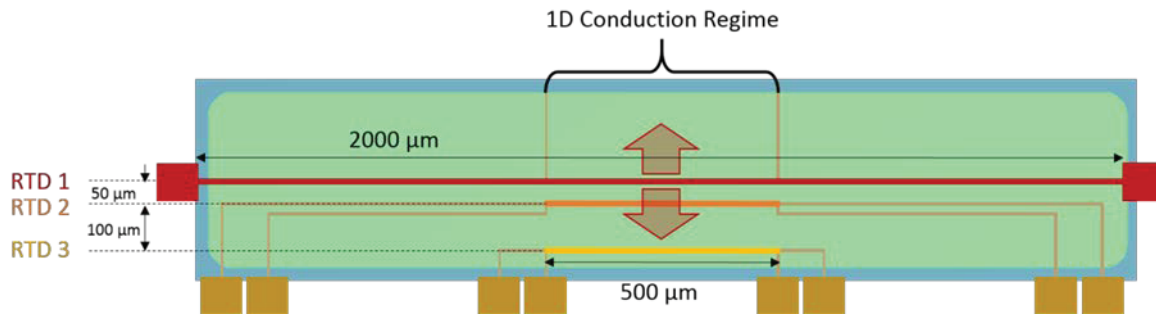
Figure 8: ERT Sample Geometry
Schematic of NCD membrane for ERT measurement. Note that the temperatures measured from RTD 2 and RTD 3 are within the 1D regime.

To experimentally measure the lateral (1D) temperature distribution of the NCD membrane during powered conditions, resistance measurements were sequentially collected from RTDs 2 and 3 while the thermal stage was held at a controlled 30°C isothermal ground condition. The

temperature of RTD 1 was derived from the driving power condition given the sourced current of 1 mA. When conducting ERT measurements in this configuration that sources a constant heat flux condition across a linear heater geometry, it is important to distinguish the nature of the temperature distribution observed across the length of the source RTD 1 during powered conditions from that observed during temperature calibration. As reported in literature by a similar resistance thermometry technique [9] and otherwise demonstrated in the FEM of the membranes measured in this work [see Figure 5(b)], the constant heat flux applied by the centerline heater creates a parabolic-like temperature profile across the NCD membrane. Therefore, the isothermal temperatures resolved using A_R are reflective of the steady-state measurement conditions from calibration and therefore are equivalent to averages of the temperature distributions spanning the lengths of the RTDs during power conditions. Thus, since the positions and lengths of RTDs 2 and 3 were confined to the 1D regime, the temperatures resolved from these RTDs were expected to most closely conform to the linear temperature distribution observed from the more locally accurate Raman thermometry measurements. The temperature resolved from the centerline RTD 1 that spanned the full length of the NCD membranes, however, was expected to underestimate the peak temperature rise predicted by the linear temperature distribution due to the inclusion of reduced temperatures near the thermally bounded end conditions since there is a parabolic temperature profile across the heater.

The lateral thermal conductivity, *kERT*, of each sample was deduced from the experimental temperature data, *Texp(ri)*, by fitting the numerical temperature solutions, *TFEM(ri)*, of a FEM of the full membrane structure, where ri denotes the ith metal line structure, *r*, on each sample. The optimal value of *k* was resolved by identifying the thermal conductivity input to the FEM that minimized the error between *Texp(ri)* and *TFEM(ri)*. To appropriately consider the temperature averaged measurements from the experiment, each temperature data point from the FEM was an equivalent spatially averaged temperature. Similar to the circumstances observed in the Raman thermometry temperature results, the temperature measured from the centerline heater (RTD 1) was excluded from the fitting algorithm for resolving *kERT* due to the experimentally observed underestimation of the peak temperature rise predicted by the calculated temperature distribution from the FEM. Although in this case when using ERT, only two experimental temperature measurements remain to characterize the linear temperature distribution observed from the FEM and used for fitting to resolve *kERT*, the exclusion of RTD 1 is a reasonable assumption for several reasons. Not only is the peak temperature measured from the centerline heater the most uncertain due to the nature of Equation 2 (where *T* is now the temperature resolved by ERT), this measurement's uncertainty is also adversely affected by the inclusion of more uncertain temperatures beyond the 1D regime and a pronounced sensitivity to the TBR between the RTD and the NCD membrane.

2.4 Uncertainty Considerations in FEM Models for Steady-State Thermometry

2.4.1 Experimental Uncertainty

The total experimental uncertainties of the lateral thermal conductivities resolved by Raman thermometry and ERT, δk_{Raman} and δk_{ERT} respectively, were determined by quantifying the (1) measurement uncertainties, δk_{meas}, due to limited measurement resolution, accuracy, and precision inherent to each experimental technique and (2) the material uncertainty, δk_{mat}, due to the material-specific uncertainties associated with the fabrication of the NCD membrane sample and the limited characterization of auxiliary material properties, and summing the two components, δk_{meas} and δk_{mat}, in quadrature.

When considering experimental uncertainty, it is critical to exhaustively consider the sources of uncertainty and to specifically distinguish the nature of each source. The magnitude of the total uncertainty in lateral thermal conductivity (irrespective of measurement technique), δk, was assessed as a combination of three natures of uncertainty: measurement resolution, accuracy, and precision. Measurement resolution is the smallest change in a measured value that can be detected using an instrument. In this work, the measurement resolutions of the Fluke 54IIB Thermometer paired with a K-type TC, the Keithley 2400 Sourcemeter, and the Agilent 34410A 6 ½ Digit Multimeter were determined according manufacturer specifications. Accuracy assesses the proximity of a measured value is to its "true" or theoretical value, where the measured value is the statistical mean of sample set of measurements. Measurement accuracy is most appreciably limited by measurement resolution and systemic errors. In this work, the spectral accuracy of the Renishaw InVia Raman spectrometer was improved to achieve an effective resolution beyond the limited resolution specified by the manufacturer by fitting a pseudo-Voigt theoretical model to the experimental spectral data. The accuracies of temperature determination according to both Raman thermometry and ERT that can easily be offset by systemic errors were improved and accounted for by calibration. Precision, often referred to as repeatability or statistical variance, assesses the degree of consistency in results that are obtained when an instrument is used to repeatedly measure the same quantity. Measurement precision is commonly limited by necessarily small measurement sample sizes that are bounded to accommodate long measurement times, and by random errors such as unaccounted fluctuations of ambient conditions. In this work, the precisions of spectral measurements collected using the Renishaw InVia Raman system, and stochastic fitting routines for resolving spectral data and lateral thermal conductivity determination were accounted for by extracting 95% confidence intervals from repeated measurement data that was assumed to have normally distributed random errors.

The uncertainties of analytically derived quantities can be resolved by propagating input measurement uncertainties according to a conventional uncertainty estimation method that uses partial derivatives of the derived functional form as sensitivity coefficients to augment a summation in quadrature. This conventional analytic method is most useful for systems of measurement that involve linear functional forms for resolving final measurement results and uncorrelated input measurements. For circumstances such as these, the summation of uncertainties may be implemented according to

$$\delta y = \sqrt{\sum_{i=1}^{n} \left(\frac{\partial f}{\partial x_i} \delta x_i \right)^2} \tag{3}$$

Approved for public release; distribution is unlimited.

where the derived quantity, y, is a function of n measured quantities, x_i: $y = f(x_1, x_2, \ldots x_n)$. For more complex systems of measurement and analysis that include partially correlated input measurements, this conventional method can become difficult and inaccurate. Alternatively, a Monte Carlo (MC) simulation method may be used to stochastically estimate the propagated uncertainty of a measurement result. The primary advantage of using a MC simulation method over the conventional analytic method is that knowledge of the functional relationships between input measurements and potential correlations between the input errors and uncertainties are not requisite to the MC uncertainty estimation [10]. A detailed development of the theoretical background, an illustration of the mechanism of uncertainty propagation, and a demonstration of the MC simulation method's compatibility with the conventional analytical method are provided in literature [11].

A combination of analytic and stochastic methods was used to quantify $(\delta k_{Raman})_{meas}$ and $(\delta k_{ERT})_{meas}$. The MC simulations used in this work iteratively perturbed the input measurement data to randomly sample each input measurement's uncertainty and yield uniquely modified experimental data sets. During each iteration of the simulation, the modified experimental data was used to fit an unknown parameter to a theoretical model by resolving the solution of minimum error. All input uncertainties and calculated errors were assumed to be randomly sampled and normally distributed. The optimal outcome for the unknown parameter and its uncertainty were respectively assessed as the mean and 95% confidence interval extracted from the normal distribution fit to the accumulation of unknown parameter outcomes. For stochastic fitting to resolve k_{Raman} and k_{ERT}, the input experimental uncertainties from each measurement technique were determined by analytical uncertainty propagation. For stochastic fitting to resolve spectral peak positions measured by the Raman spectrometer, the input spectral uncertainties were determined according the manufacturer-specified resolution of raw spectral data (not yet fit to theoretical model).

The material uncertainties, δk_{mat}, contributing to δk_{Raman} and δk_{ERT} were attributed to the experimental uncertainties in determining the material layer thicknesses and auxiliary material properties listed in Table 1. Because each of these parameters' analytical correlation to k is obscure and impractical to resolve analytically, their respective uncertainties would be most effectively propagated via MC simulation. However, due to the high computational cost associated with repeated sampling of the FEM for numerous input paramaters, the contributions of each parameter were determined by varying each parameter independently by its respective experimental uncertainty in the FEM and assessing the resulting error in lateral thermal conductivity according to

$$\delta k_{mat} = \sqrt{\sum_{i,j} \delta k_{i,j}^2} \tag{4}$$

where $\delta k_{i,j}$ is the error in thermal conductivity, resulting from varying FEM input parameter, i, according to variation conditions j.

2.4.2 Modeling Error

Although experimental uncertainty is typically the most commonly considered measure of inconsistencies in experimental results, even a perfectly accurate and precise measurement has the potential to lead to an inaccuracy when comparison to a theoretical model is involved in obtaining the desired measurement result. This inaccuracy given a perfect experimental measurement, herein termed modeling error, is due to the assumptions of the theoretical model that necessarily approximate the conditions of the inherently imperfect experimental materials and conditions.

For lateral (in-plane) thermal conductivity measurement of NCD suspended membranes via the steady-state techniques demonstrated in this work, the most notable artifact of modeling error was the discrepancy between the experimentally measured and numerically modeled (FEM) peak NCD membrane temperatures. To approximately hypothesize the effects of convective and radiative losses due to ambient conditions, a simplified comparative analysis has been performed for the NCD membrane dimensions used in this work. Consider the NCD membrane with the following coarse assumptions to: be a rectangular membrane with length L of 2000 μm, width W of 400 μm, and thickness t of 1 μm; have lateral 1D conduction across the entire membrane; and have an isothermal surface temperature equal to that of the peak temperature predicted by the FEM. If effective heat losses due to radiation with emissivity ε of 1 and convection due to free convection above a flat plate and enclosed in a rectangular cavity (to approximate beneath the NCD membrane) in ambient air are considered, the total heat losses due to convection and radiation have been analytically approximated to be ~14.5% and ~0.5% respectively. These are gross approximations with an isothermal surface temperature approximately equal to the peak temperature of 110°C estimated by the FEM and that most clearly provide an order of magnitude understanding of possible heat losses experienced during powered heater conditions on the NCD membrane. For isothermal surface temperatures measured at a lateral distance of 100 μm from the centerline heater that are approximately equal to 60°C, these convective and radiative losses reduce to ~5% and ~0.2% respectively and can be treated as negligibly affecting conduction through the NCD membrane. Therefore, the aforementioned exclusion of temperature measurements in lateral proximity of the centerline heater successfully negates any potential effects of convective or radiative losses experienced at elevated membrane temperatures.

Another prominent contributor to modeling error in the Raman thermometry and ERT techniques demonstrated in this work that can potentially affect lateral thermal conductivity results is the assumed temperature independence of the NCD membrane lateral thermal conductivity. This assumption has been experimentally confirmed to negligibly affect the samples measured in this work by performing ERT measurements for varying source heater power conditions. By incrementally varying the source power from 25 mW to 221 mW and fitting each set of experimental results to resolve lateral thermal conductivity for each power condition, the lateral thermal conductivity is observed to clearly converge to the reported lateral thermal conductivities [see Figure 9].
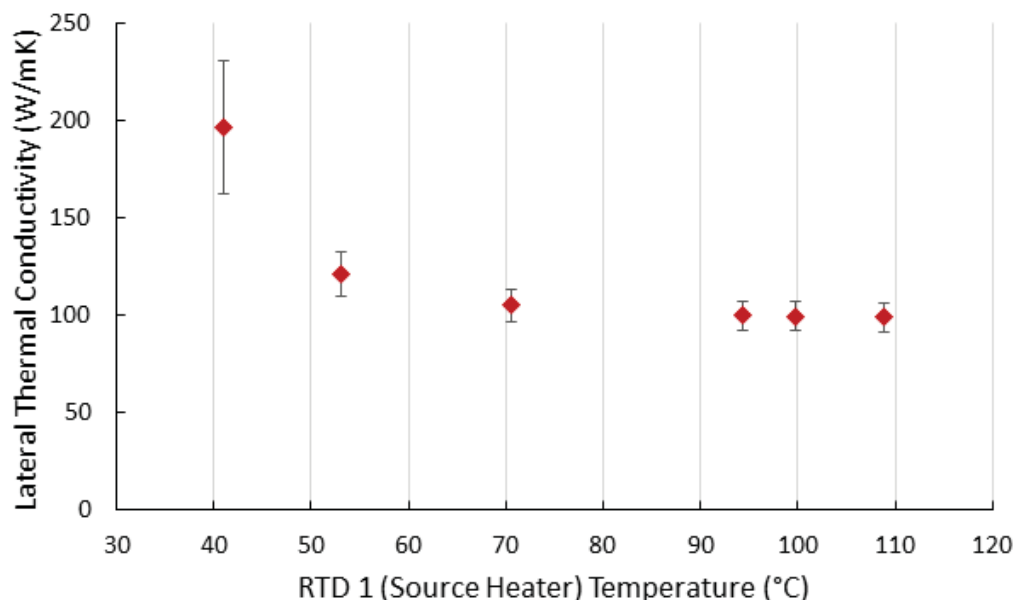
Figure 9: Thermal Conductivity as a Function of Heater Temperature
Lateral thermal conductivity temperature dependence of NRL 010516 A5 M1 as measured by ERT.

2.5   Raman and ERT Results

The experimental results obtained from the four membrane samples: NRL 010516, Die A5 (common sample) and membranes M1 and M2, and NRL 122315, Die E3, and membranes M1 and M2 are shown in Table 1 accompanied by the experimentally measured auxiliary material properties used to construct the FEM analysis. The thermal conductivity results from both measurement techniques show strong agreement for membranes measured on the same sample, illustrating minimal deviation between thermal conductivities deduced by the methods and across the sample die. It is also important to note that lateral thermal conductivity results resolved from both Raman thermometry and ERT are membrane-averaged thermal properties (e.g., not local property measurements). The results also show an improvement in thermal conductivity of 23 W/mK was measured from samples grown with 40 nm diamond seeds (NRL 122315, Die E3) with respect to the 4 nm seeded sample (NRL 010516, Die A5). The NCD membrane and Al layer thicknesses, t_{NCD}, were measured via transmission electron microscopy (TEM).

The thermal conductivity of the Al thin films was determined by measuring the electrical conductivity and hence calculating the thermal conductivity according to the Wiedemann-Franz law. The thermal interface conductances, $G_{RTD/NCD}$, $G_{NCD/Al}$, and $G_{NCD/Si}$ were measured via TDTR. The experimental Raman thermometry results for NRL 010516 Die A5 and membrane M1 are shown in Figure 10 and are exemplary for the Raman thermometry technique. The experimental ERT results for samples NRL 010516 Die A5 and membrane M2 and NRL 122315 Die E3 and membranes M1 and M2 are shown in Table 2. ERT measurements are not presented for NRL 010516 Die A5 membrane M1 due to metal heater structure damage incurred during measurements that left the sample electrically inoperable.

Table 1. Fitting Parameters and Properties of CVD Diamond Membranes

	NRL 010516 A5 M1 (4 nm seeds) 200 mW	NRL 010516 A5 M2 (4 nm seeds) 200 mW	NRL 122315 E3 M1 (40 nm seeds) 200 mW	NRL 122315 M2 (40 nm seeds) 200 mW
k_{Raman} (W/mK)	**100 ± 5 (5%)**	-	**122 ± 6 (5%)**	-
k_{ERT} (W/mK)	-	**99 ± 7 (7%)**	**123 ± 6 (5%)**	**123 ± 6 (5%)**
t_{NCD} (μm)	1.06 ± 0.02 (2%)	1.06 ± 0.02 (2%)	1.06 ± 0.02 (2%)	1.06 ± 0.02 (2%)
t_{Al} (nm)	92.3 ± 5.3 (6%)	92.3 ± 5.3 (6%)	100 ± 5 (5%)	100 ± 5 (5%)
k_{Al} (W/mK)	175 ± 9 (5%)	175 ± 9 (5%)	175 ± 9 (5%)	175 ± 9 (5%)
$G_{RTD/NCD}$ (MW/m²K)	169 ± 15 (9%)	169 ± 15 (9%)	169 ± 15 (9%)	169 ± 15 (9%)
$G_{NCD/Al}$ (MW/m²K)	147 ± 17 (12%)	147 ± 17 (12%)	129 ± 6 (5%)	129 ± 6 (5%)
$G_{NCD/Si}$ (MW/m²K)	70 ± 14 (20%)	70 ± 14 (20%)	70 ± 14 (20%)	70 ± 14 (20%)

Lateral thermal conductivity values (bold) fit using the finite element model applied to the Raman and ERT data, along with the auxiliary material property measurement results for membranes 1 and 2 from samples NRL 010516 A5 and NRL 122315 E3. The power sourced to the centerline heater is noted.
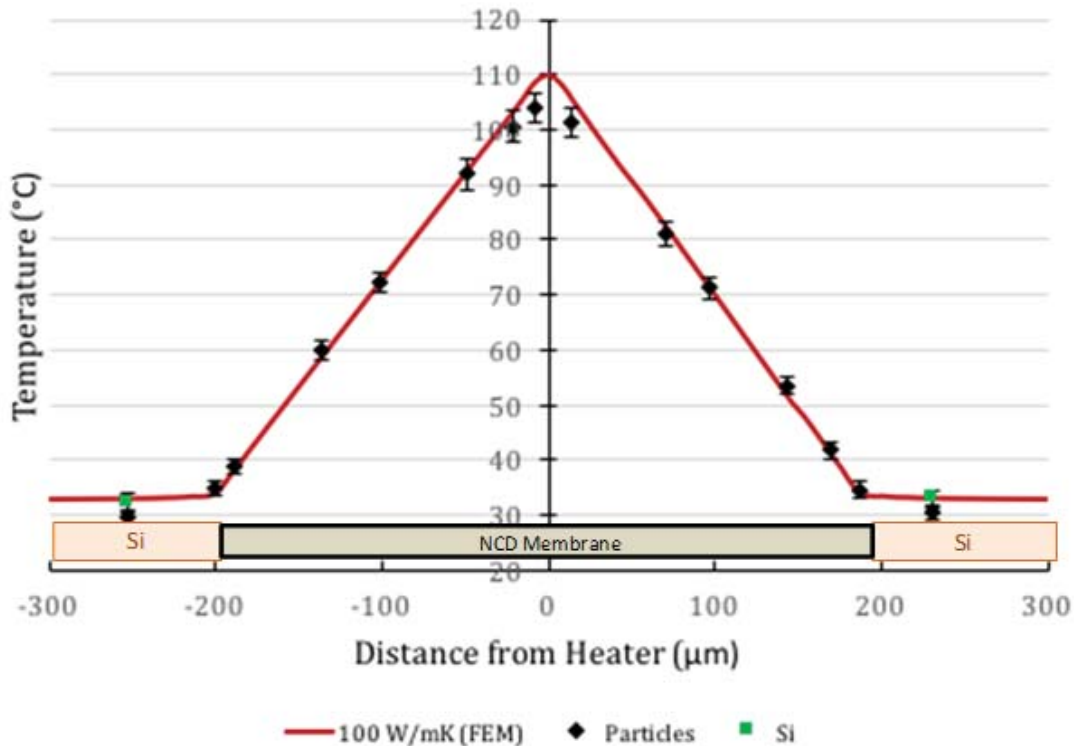
Figure 10: Temperature Distribution and Model Fit to Profile across Diamond Membrane
Experimental temperature distribution as measured by Raman thermometry for NRL 010516 Die A5 membrane M1.

16
Approved for public release; distribution is unlimited.

Table 2. Temperature Distribution during ERT Measurements

	NRL 010516 A5 M1 (4 nm seeds) -	NRL 010516 A5 M2 (4 nm seeds) 194 mW	NRL 122315 E3 M1 (40 nm seeds) 200 mW	NRL 122315 E3 M2 (40 nm seeds) 200 mW
RTD 1 (Heater) (°C)	-	99.8 ± 2.1	85.6 ± 2.1	86.8 ± 0.9
RTD 2 (°C)	-	87.7 ± 2.9	81.8 ± 2.0	81.9 ± 1.0
RTD 3 (°C)	-	49.3 ± 0.8	50.1 ± 1.3	50.0 ± 0.5

ERT temperature results for the measurements conducted on samples: NRL 010516 A5 M2 and NRL 122315 E3 M1 and M2. The power sourced to the centerline heater (RTD 1) is noted.

2.6   Time-domain Thermoreflectance

Nonhomogeneous and anisotropic thermal conduction in these nanocrystalline chemical-vapor-deposited diamond films was also investigated by TDTR. TDTR is a pump-probe photo-thermal technique that employs an ultra-fast laser to heat a sample and then measure the temporal response of the surface temperature over a few ns [12,13]. This technique is well-established for measuring cross-plane and in-plane thermal conductivity and TBR in multilayer thin-film structures [6]. These measurements were performed by both the Georgia Tech (GT) and Stanford research groups with similar approaches taken by each group with a typical setup shown in Figure 11. The pump (heating) pulse is modulated in the range of 1-10 MHz using an electro-optic modulator (EOM), which not only controls the penetration depth of the thermal wave into the sample, but also allows a lock-in amplifier to extract the temperature response of the surface with a much higher signal to noise ratio. The probe (temperature sensing) pulse travels through a mechanical stage that can delay the arrival of the probe relative to the pump pulse over a range of 0.1 to several ns, which is how a temperature decay curve is captured. The maximum delay time is 7 ns using a double-pass delay stage.

One important aspect of this technique is that it requires a metal transducer to be deposited on the surface of the sample to allow for sufficient resolution in determining the temperature decay. The temperature of the sample is sensed by measuring the change in reflectivity of a thin metal layer on the sample surface. Due to the large surface roughness present on the growth side of the diamond films (Figure 1), the aluminum transducer layer required for the TDTR measurements was deposited on the nucleation side (i.e., where the silicon substrate was etched away) where the roughness is considerably lower. Al is used as the transducer due to a high thermoreflectance coefficient at the probe wavelength [12].

The measurement of the thermal properties of the sample are also quite sensitive to the properties of this transducer layer, including the metal/sample TBR, metal thermal conductivity, and metal thickness. To minimize variations between the groups, all metal transducers (~ 90 nm Al) were deposited by the Naval Research Laboratory (NRL) so that both teams would have the same starting material. For the GT team, the thermal conductivity of the Al layer was measured independently and the thickness verified on the sample using picosecond acoustics due to the shorter laser pulse width at GT [13]. This film thickness was then shared with Stanford for data analysis. Using these methods, we were able to verify the film thickness deposited by the NRL.
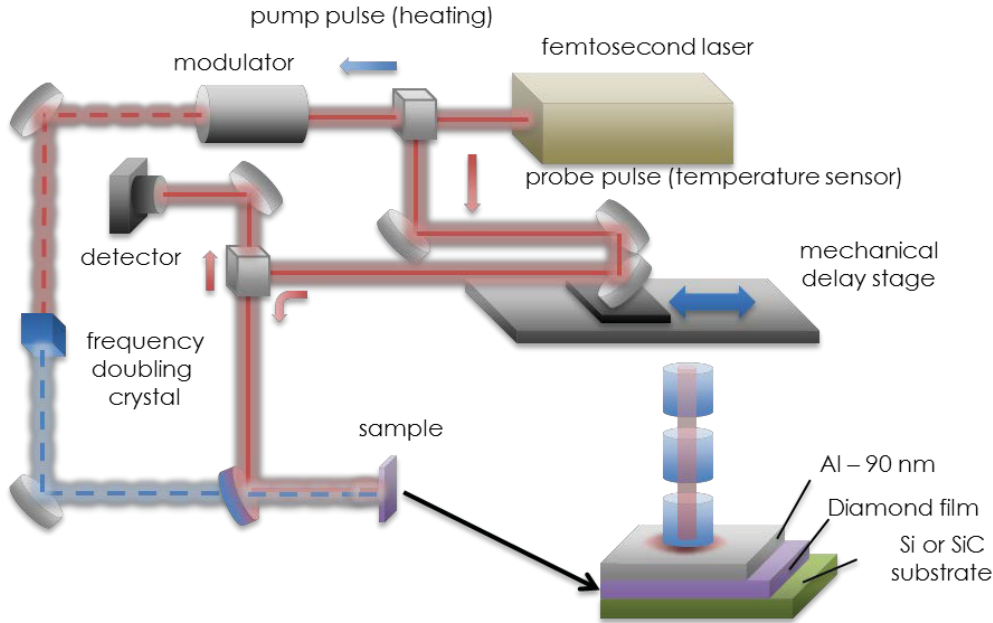
Figure 11: TDTR System
Depiction of the pump-probe TDTR system for measuring the thermal properties of samples studied in this work. As an example, a sample of thin film CVD diamond deposited on a silicon or silicon carbide substrates is shown complete with an aluminum (Al) transducer layer on top to facilitate the thermoreflectance-based measurement.

Parameter estimation for the films was performed by fitting an analytical solution to the transient heat conduction in the sample to the experimental data, allowing robust parameter determination as well as uncertainty and sensitivity analysis. In addition to using simultaneous multi-frequency fitting of parameters, the GT group employed MC sampling of the uncertainty in the input parameters to provide additional assessment of the uncertainty on the estimated thermal properties [10].

By performing a sensitivity analysis prior experimentation, we designed sample geometries to maximize the measurement sensitivity to the desired properties, and also identify the major factors that dominate the uncertainties in the extracted properties. Figure 12(a) shows the representative sample geometry of interest for the TDTR sensitivity analysis, while Figure 12(b) plots the relative sensitivity of the thermal model to various thermophysical parameters of interest as a function of thermal diffusion time, including the in-plane thermal conductivity of the diamond, as well as the thicknesses of both the diamond and aluminum thin films. As a general rule, the larger the sensitivity of the model to perturbations in a given parameter of interest, the better suited that measurement will be for making an accurate determination of that thermophysical property.

An alternative way for assessing the sensitivity of these thermophysical properties across a wider sample property space is to evaluate based on the average sensitivity. We define the average sensitivity for a TDTR measurement as:
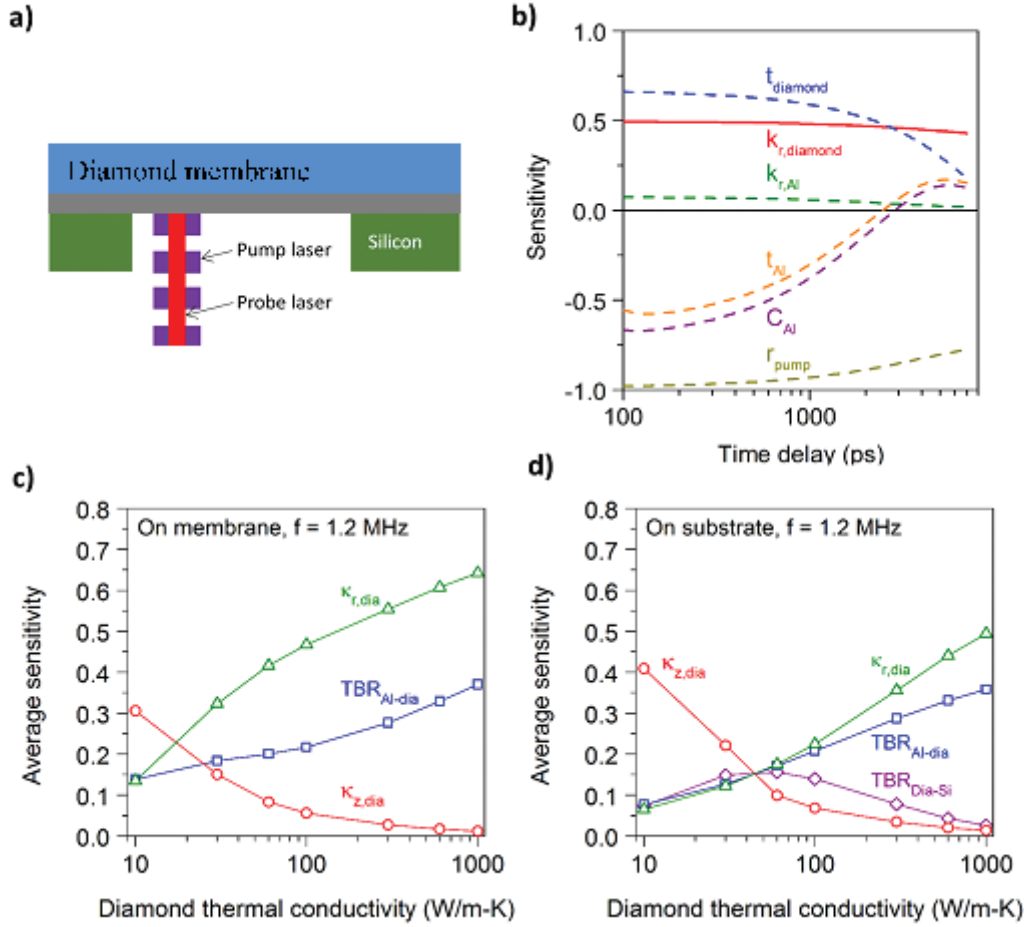
Figure 12: TDTR Measurement and Measurement Sensitivity on Diamond Membrane
TDTR In-plane measurements: (a) Sample geometry for suspended membrane measurement. (b) Sensitivity of TDTR measurement to input parameters. (c) Average sensitivity to κ_r for different values of κ_r at heating frequency of 1.2 MHz for 1.1 μm suspended diamond film. (d) Average sensitivity to κ_r for different values of κ_r at heating frequency of 1.2 MHz for 1.1 μm diamond film on Si.

$$S_{p,avg} = \frac{1}{N}\sum_{i=1}^{N}\left|\frac{dR/R_i}{dp/P_i}\right| \tag{5}$$

where R is the measured ratio of in phase temperature signal to out of phase temperature signal $(-V_{in}/V_{out})$ and p is the value of the property of interest, and $S_{p,i}$ is defined in previous literature [23]. The average sensitivity provides a single sensitivity value for the entire time region of measurement to allow direct comparison of the ability to resolve different unknown parameters with the measurement. Taking the average sensitivity over the entire delay time is a more accurate method of comparing sensitivity rather than choosing a specific delay time. Figure 12(c) shows how the average sensitivity to the unknown parameters in the suspended diamond film vary as the thermal conductivity of the diamond varies. In these cases, the dependent

19
Approved for public release; distribution is unlimited.

variable represents an isotropic thermal conductivity where both κ_z and κ_r are increasing together. Even for relatively low κ_r values of 30 W/m-K, the average sensitivity is above 0.3, which is acceptable for a measurement; however, the measurement is ideally suited to κ_r of 100 W/m-K and higher where the sensitivity to κ_r is above 0.4 and the sensitivity to κ_z is below 0.1. Although the sensitivity to the Al-diamond TBR also continues to increase with κ_r, it is most sensitive at 3-7 ns, while the measurement is sensitive to κ_r during the short times (0.1-3 ns). In this scenario, we can still independently fit for κ_r and TBR$_{Al\text{-}dia}$ with a single measurement. In comparison to the measurements on a substrate (Figure 12(d)) the membrane measurement is around 30% more sensitive to κ_r; in addition the unknown parameter TBR$_{Dia\text{-}Si}$ is removed further increasing the accuracy of the membrane measurement. Both groups have validated system and data reduction accuracies by extracting room-temperature thermal conductivity of a single crystalline sapphire (Al$_2$O$_3$) calibration sample and an intrinsic single crystalline Si calibration sample, each of which is within 2% of reference literature values for bulk single crystalline sapphire and silicon. It was also determined that TDTR was best performed on samples with surface RMS roughness less than 50 nm.

Based on the assessment from the sensitivity analyses, heating frequencies of 1.2 and 2.2 MHz were used to ensure that the 1 µm film is fully penetrated, thereby ensuring that the measurement is insensitive to the through-plane diamond thermal conductivity ($\kappa_{z,dia}$) [16]. Furthermore, we use the low heating frequency and a small spot size (1/e^2 diameter of 10/4 µm for pump/probe) to allow the heat to diffuse outside of the laser spot size laterally, which enhances the sensitivity to $\kappa_{r,dia}$. As shown in the sensitivity analysis, the ability to measure the in-plane thermal conductivity of any film with TDTR is highly dependent upon the in-plane thermal conductivity value of that film. The thermal conductivity must be large enough so that the heat can diffuse laterally away from the sensing laser beam within the time scales of the measurement. As the measurements are very sensitive to the diamond thickness, Al heat capacity, diamond heat capacity, and laser spot size, these parameters must be well-known. The thickness of the diamond is measured using ellipsometry, and the laser spot sizes are measured using a beam profiler. The heat capacity of Al is taken to be 2.43 MJ/m^3-K from literature [14], while the diamond heat capacity was measured experimentally. The heat capacity of diamond is strongly dependent on temperature near room temperature due to its extremely high Debye temperature [15]. We place the sample in a cryostat to change the sample temperature and then use very low power and multiple frequencies extract heat capacity separately from thermal conductivity [16]. The resulting expression for heat capacity $C_{dia}(T) = 1.096 \times 10^{-2}T - 1.503$ where T is in K and C is in MJ/m^3-K are in good agreement with previous measurements on nanocrystalline diamond [17], but are only meant to describe the heat capacity at and slightly above room temperature.

2.7   Measurements Summary and Discussion

The data from measurements on both the 4 and 40 nm seed diamond membranes using all three techniques are summarized in Table 3. For each sample, the measurements made using the various techniques all compare quite well. In the case of the sample fabricated using the 4 nm seeds (010516, coupon A5), the thermal conductivity ranges from 95 to 98 W m-1 K-1, with an average uncertainty of 12-15%. Similarly, the values measured on the 40 nm seed sample (122315, coupon E3) also compare well, ranging from 120 to 132 W m-1 K-1 with uncertainties around 10-15%. Also included in Table 3 are measurements made on the same samples by other Universities in the program, further validating the values measured at GT.

Table 3. Thermal Conductivity of Diamond Samples Measured by Multiple Universities

Lateral k (W/mK)	Georgia Tech			Bristol	Stanford	Tx State
Sample	TDTR	Raman	Electrical Resistance	Raman	TDTR	Raman
NRL 010516 A5	95 ± 14 (M1)	103 ± 15 (M1)	98 ± 12 (M2)	90 ± 2 (M1)	-	90 (+13/-11)
NRL 122315 E3	132 (+12/-22) (M1)	120 ± 17 (M1)	128 ± 16 (M1) 128 ± 16 (M2)	-	135 ± 12	

One of the important aspects of the results in Table 3 is the consistency in the measured values made via both global and local techniques. The Raman and ERT measurements are global in the sense that they are an average over the thickness and width of the membrane. In contrast, the TDTR measurement is local in that it samples a specific point; the heating spot has a diameter of 10 μm and the thermal diffusion length is ~3 μm in the lateral direction, resulting in a 2D heating area 16 μm in diameter. The small sampling volume of TDTR has both advantages and disadvantages; the small spot size allows spatial mapping and determination of local thermal properties, which is good for understanding the fundamental behavior of the material but can be less ideal when trying to get an average property of a highly inhomogeneous thin film. Regardless, the agreement between the TDTR scans and steady-state techniques highlight the homogeneity of the diamond microstructure within the membranes.

Given the consistency between the various techniques, the differences in the thermal conductivities of the two thin films fabricated using different seed sizes can be readily observed. The sample fabricated using the 40 nm seeds show a clear improvement in the overall thermal conductivity of the film compared to using a 4 nm seed. These differences in thermal conductivity can be attributed to the differing microstructures of the CVD diamond, which result due to the choice of seed size. The smaller seeds result in smaller grains within the diamond thin film. As a result of these smaller grains, there are more grain boundaries to act as phonon scattering sites within the thin film, thereby reducing the thermal conductivity compared to films with fewer boundaries. Therefore, these results suggest that in order to maximize the thermal conductivity of diamond thin films, larger diamond seeds should be used as nucleation sites for CVD thin film growth.

Now that they consistency between the test methods has been demonstrated, it is imperative that we discuss the merits of each for measuring various thermal properties in CVD diamond films. It should be noted that with sufficient effort, excellent and consistent thermal properties can be obtained out of the technique that we have studied. However, not all methods are equal in terms of the level of effort and speed needed to make thermal property measurements. For instance, all samples need relatively low surface roughness to make the metal/diamond contact sufficient for heater operation or for TDTR reflections. As demonstrated in this study, most samples also need

microfabrication to create membranes for 1D heat flow analysis. It is possible to measure some film on substrate samples using techniques like TDTR, 3-omega, or nanoscale thermoreflectance methods, however the restriction of low surface roughness samples remains (<30 nm rms). Methods like TDTR require more proficient users to ensure that the systems are well calibrated and aligned whereas methods like ERT can be easily translated to technicians without months of training to keep the system in top shape. However, it does require expertise on the data analysis side which utilized FEM analysis to extract thermophysical properties. Nonetheless, ERT was found to be the fastest of all measurement capabilities for lateral thermal conductivity when sample membranes could be created. Measurements were a factor of 10-20 times shorter than that of Raman measurements. Table 4 summarizes the three main techniques studied in this program and how well they rate for performing thermal conductivity measurements.

Table 4. Summary of the Comparison between Test Techniques for Thermal Conductivity Measurements

Desired Quantity	Raman	TDTR	Electrical Resistance
Thick diamond – k	*	●●	●● (using 3□)
Thin membrane – Lateral k	●●	●●	●●
Thin diamond – Vertical k	●	●	----
Thermal Interface Resistance	*	●● (nanosecond)	----
Mapping spatial variation of k	*	●●	----
Measuring k if C_p is unknown	●●	●	●●
Device Temperature	●●	----	●●
Speed of measurement	●	●	●●
Ease of sample prep	●	●	●

Key:
---- measurement not practical
● measurement possible but not ideal
●● high quality measurement demonstrated under this DARPA program
* measurements demonstrated outside of this DARPA program

Approved for public release; distribution is unlimited.

3. Impact of Interface Composition and Structure on Thermal Boundary Resistance

Additional work conducted during this reporting period included the characterization of the TBR at heterointerfaces between CVD diamond and various materials. Previous studies performed as part of the Near Junction Thermal Transport (NJTT) program through the DARPA were able to achieve a 2.7X reduction in the thermal resistivity of a HEMT device compared to a GaN-on-SiC device, and also demonstrated a 3X increase in the areal dissipation density of GaN-on-diamond comparative with GaN-on-SiC. It was found that the relatively large TBR of 47.6 m^2K/GW was a significant factor in limiting the device performance [18]. It is therefore desirable to better understand how the composition and structure of the interfacial region contributes to the overall TBR of a material-on-diamond interface.

3.1 Interfacial Compositions that Lower Thermal Boundary Resistance

In this study, TDTR was used to evaluate the TBR of three different GaN-on-diamond interfaces. The interfaces of interest consisted of diamond-on-GaN grown with a nominal 5 nm SiN interfacial layer, a nominal 5 nm AlN interfacial layer, and a diamond-on-GaN grown with no interfacial layer. These samples were all prepared in a similar fashion, to be discussed in more detail, and henceforth will be referred to as samples S, A, and G respectively. Additionally, scanning electron microscopy (SEM), TEM, and ultraviolet (UV) Raman was used to better understand and characterize GaN-on-diamond interfaces with different dielectric layers. The goal of this study was to better understand how interfacial layers and resultant composition in the interfacial region impact thermal transport at GaN-on-diamond heterointerfaces.

The samples used in this study were all grown using a microwave plasma CVD system and the nucleation of the diamond was carried out prior to the actual CVD diamond growth. During the diamond growth, all three samples were loaded into the reactor at the same time to ensure consistency among the samples. The growth of the diamond took place on three separate structures, one with a thin nominal 5 nm SiN interfacial layer, another with a nominal 5 nm AlN interfacial layer, and lastly a sample with no interfacial layer. These structures were grown on a 4H-SiC wafer with a 20 nm AlN nucleation layer and a nominal 500 nm GaN layer. Details for each of the structures can be seen in Figure 13. For all cases, the diamond growth on the GaN was successful despite the differing interfacial conditions.
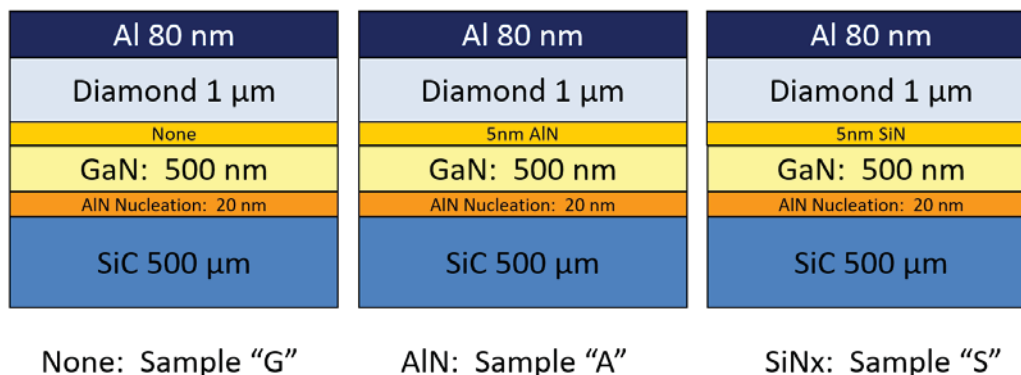
Figure 13: GaN on Diamond Samples
Sample structures investigated in this study with nominal thickness values. All samples had an additional 80 nm aluminum transducer layer deposited onto the surface of the diamond to facilitate the TDTR measurement.

To assess the TBR at the diamond/GaN interface, TDTR was used. As was the case for measurements of the in-plane thermal conductivity of the CVD diamond membranes, a thin aluminum transducer is deposited onto the surface of these samples to absorb the laser energy and provide the thermoreflectance signal via a photodiode connected to a lock-in amplifier. A radially symmetric model of heat diffusion through multiple layers is then used to fit thermal parameters to the experimental data and additional details of the setup can be found in the following reference [19].

Results of the experiments are shown in Figure 14. For sample G (no interlayer) the TBR was found to be 42 ± 13 m^{2}K/GW with some spot to spot variation. Samples A and S demonstrated a much lower spot to spot variation, and multiple measurements resulted in fit values of 17.2 ± 2.6 m^{2}K/GW and 11.4 ± 1.7 m^{2}K/GW, respectively. Sample S with the 5 nm SiN interlayer demonstrated the lowest TBR of the three samples.
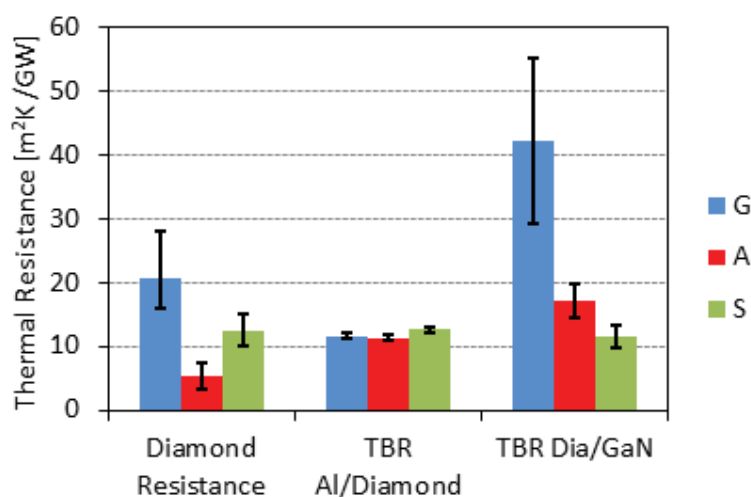
Figure 14: TDTR Measurement Results for GaN on Diamond
Measured thermal resistance of each of the fit parameters in the TDTR model
It should be noted that a similar study was carried out on GaN-on-diamond samples that were

Approved for public release; distribution is unlimited.

analyzed by Gu *et al*. using a non-contact transient reflectance method that is matched to FEM simulations at the University of Bristol [20, 21]. In their analysis, they found a similar trend, albeit different values on samples with different architectures. For the sample G configuration, they report values ranging from 65-85 m^2K/GW, sample A has reported values from 10-18 m^2K/GW, and sample S has values reported between 2.5-6.2 m^2K/GW. While the trend is similar, it is difficult to directly compare the values with results presented here due to several key parameters such as diamond thickness that are not specified. A more recent publication by Zhou *et al*. [22] used the same transient reflectance technique as Gu *et al*. [20] and utilized samples very similar to this work. The results obtained by Zhou *et al*. are consistent with those found in this work and demonstrate the importance in better understanding the role dielectric layers used to facilitate direct growth of diamond on GaN have in contributing to the TBR of the interface. For the results acquired in this study, error analysis was carried out using a MC technique in which all the model parameters are assigned an uncertainty, and the parameter values are randomly varied according the specified uncertainty, then the experimental data is fit to the new model. This is performed 1000 times and a normal distribution is acquired. For our reported values, we take the 50th percentile, and error bars are acquired using the 10th and 90th percentile of the normal distribution. This method for error analysis has been documented extensively in the following reference [19]. Results for the three samples are displayed in Table 5.

UV Raman measurements were carried out on the three samples, and demonstrated similar diamond qualities by observing the FWHM of each of the samples for the diamond peak shift located at 1332 cm^{-1}. All three samples also demonstrated amounts of non-diamond carbon indicated by the broad peak centered around 1580 cm^{-1}. A significant difference however is the lack of a second order Raman scattering of the A1 longitudinal optical (LO) mode in the GaN. This optical overtone in GaN has been studied by Siegle *et al*. [23] and provides an indication of poor contact between the GaN and diamond for sample G. Results of the Raman analysis are shown in Figure 15.
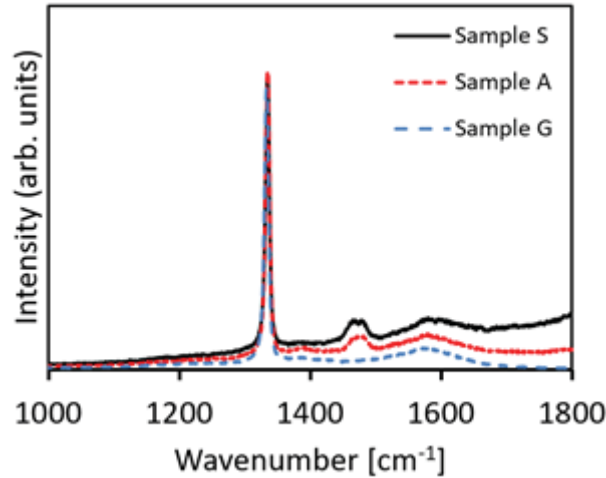
Figure 15: UV Raman of CVD Diamond Samples
UV Raman spectra of the three samples analyzed in this study. It is clear that for sample G there is no 2A1 LO peak present.

Table 5. Data for GaN on Diamond Samples

Sample	$k_{\square}$[W/m-K]	$k_{\parallel}$ [W/m-k]	d [μm]	Diamond/GaN TBR [m^2K/GW]
G	70 +20/-19	130 ± 13	1.43 ± 0.14	42 ± 13
A	206 +142/-59	130 ± 13	1.1 ± 0.11	17.2 ± 2.6
S	120 +29/-21	130 ± 13	1.5 ± 0.15	11.4 ± 1.7

Results of fit parameters for Samples G, A, and S. $k_{\parallel}$ was held constant according to reference [24]. Diamond thickness (d) was acquired from TEM imaging. $k_{\perp}$ and TBR are fit parameters.

To better explain the differences seen in the TDTR and Raman experimental results, SEM and TEM imaging was carried out. The results of these experiments demonstrated drastic differences at each of the interfaces. For the sample with no interfacial layer between the diamond and GaN, sample G, it was apparent that there was significant delamination of the diamond from the GaN layer after growth was completed. In areas where there was no delamination, extensive deterioration was visible in the form of voids measuring approximately 50 nm or more at the diamond/GaN interface. The void formation at the interface due to selective etching of the GaN during the nucleation was most likely caused by a growth environment containing hydrogen (H_2) at elevated temperatures. It is well understood that at elevated temperatures H_2 can react with the nitrogen in the GaN to form ammonia (NH_3), therefore at areas where dislocations are present, the H_2 will react with the nonpolar facet of the GaN, and begin to etch cavities into the GaN. This effect has been studied in detail by Yeh *et al*. [25]. In the case of sample A, we saw a significant reduction in the GaN thickness from a nominal value of 500nm. Bright field scanning transmission electron microscope (STEM) images indicated that the thickness of the GaN was around 255 nm, and the first 30 nm appeared to be significantly roughened. Further investigation of electron energy loss spectroscopy (EELS) scanning in the region between the GaN and diamond found no evidence of Al from the AlN adhesion layer in the area with a reduced GaN thickness. However, this sample showed the formation of mesa structures at the GaN/diamond interface, indicating a non-continuous AlN layer and etching of the GaN. For sample A, the AlN formed in select regions of the GaN. This is apparent in Figure 10b from the much smoother interface on the top of the mesa structure compared to that of the etched region, as well as the inclusion of voids in this region. In this scenario the AlN is acting as an etch barrier, but because the AlN layer is non-continuous, the harsh diamond growth environment etches the exposed GaN similar to sample G, and creates a significantly roughened surface. Even though there was significant etching of the GaN, the two materials appeared to remain in intimate contact (Figure 16a), as there were no obvious signs of delamination of the diamond layer. Additional low voltage dark field STEM did reveal small voids at the diamond/GaN interface as seen in Figure 16b. This sample did demonstrate a lower TBR compared to sample G (Figure 13), due to the smooth interfaces where the AlN was present, and the better adhesion of the diamond film. The TDTR measurement utilized a spot size with a 40 μm diameter, so it is likely that the measurement area encompassed both regions of the interface.
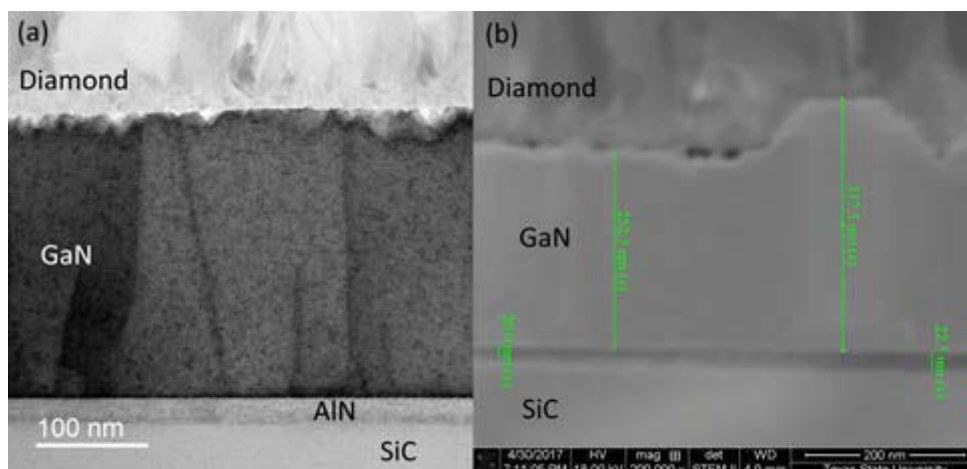
Figure 16: TEM Images of GaN-Diamond Samples
(a) Sample A TEM image showing good contact between the diamond and GaN with significant roughening of the interface. (b) SEM image of sample A showing small voids at the interface, and demonstrating etching of the GaN where no AlN barrier is present.

For sample S, a 3nm wide amorphous region was identified using bright field STEM, and can be seen in Figure 17a. The diamond lattice planes can be clearly seen in the region above the amorphous layer. An EELS spectrum from the amorphous region is shown in Figure 17b and clearly indicates the presence of Si, C, and N. To better understand the structure of the SiN interlayer, high angle annular dark field (HAADF) imaging was performed in order to extract a 5x7 nm area in which the relative component contributions are captured (Figure 18).
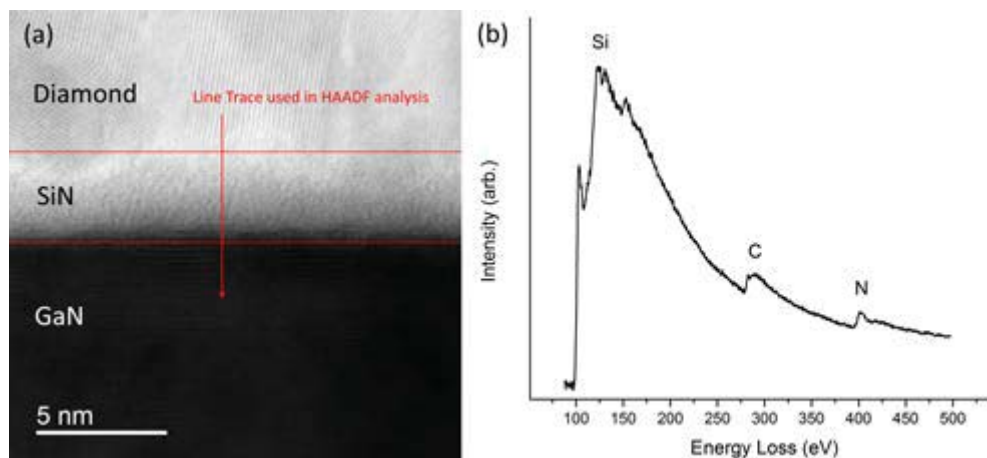
Figure 17: TEM and EELS Imaging of GaN-Diamond Interface with SiN Interlayer
(a) High resolution TEM of sample S showing the diamond lattice planes and a ~3 nm of SiN acting as an etch barrier. (b) EELS spectrum of sample S showing the presence of Si, C, and N.

The spectra were smoothed using principle component analysis using Hyperspy [26]; with a 5-component model, elemental mappings were created by integrating the Si L2,3,C K, and N K edges. The lighter region at the bottom of HAADF image marks the top of the GaN layer.

Quantification of the composition was done using the original, un-smoothed data taken from a vertical line running through the center of the image. Compositions were determined by calculating the integrated intensity of the edge after power law background subtraction. Compositions were then determined using cross sections calculated by Egerton's SigmaK3 and SigmaL3 codes [27]. For verification, the composition of the SiC substrate was measured and found to be 51.4% Si and 48.6% C.
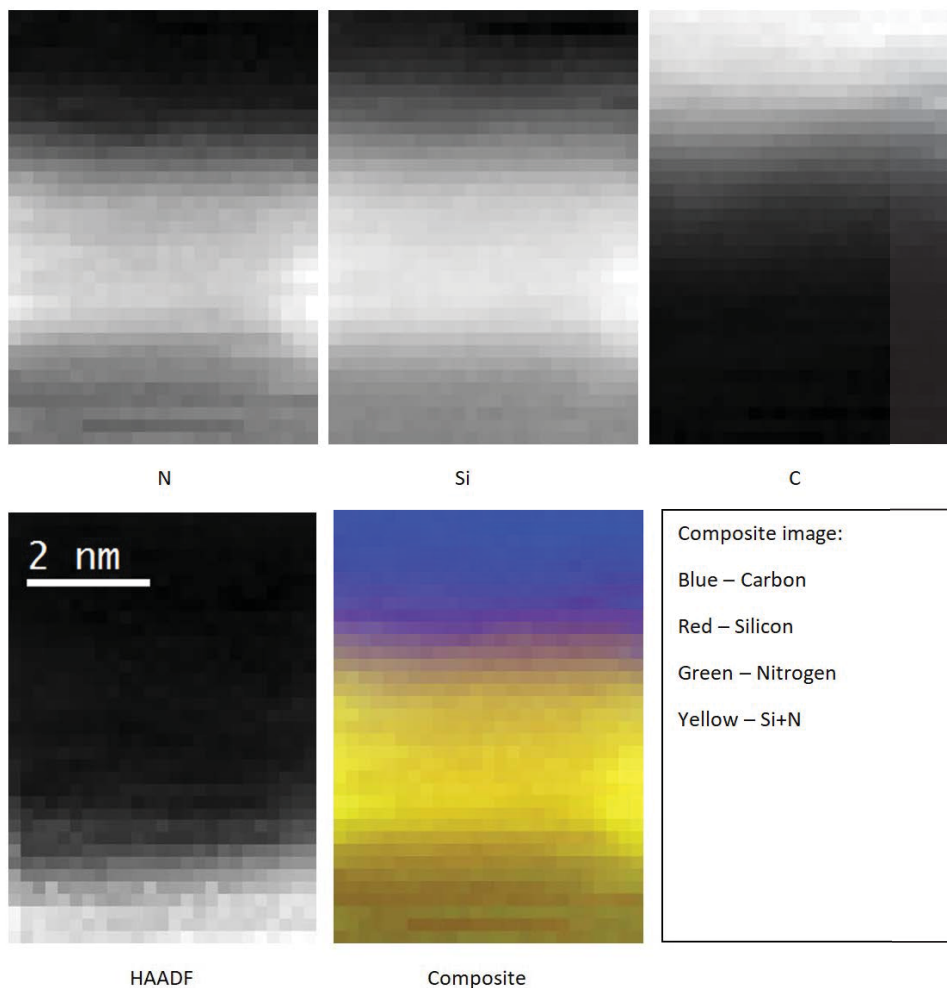
Figure 18: HAADF Imaging of GaN-Diamond Interface with SiN Interlayer
(Top row) Relative contributions of N, Si, and C across the interface (lighter areas indicate higher concentrations of the particular element). (Bottom row) Complete HAADF image with an overlaid composite image consisting of all elements as defined by the referenced colors

The composition mapping begins in the diamond and shows the changes moving across the interfacial layer into the GaN. There is a gradual decrease in the C composition over a range of about 4 nm. Over this same region the content of both Si and N increases in a nearly one-to-one ratio. The HAADF image indicates that the last 1 nm of the scan is in the GaN, but the EELS data shows a significant Si content. This is shown in Figure 19a, and it is important to note that the composition calculations don't take into account the Ga in this region, here the percentage is based on the Si:N ratio. However, in a separate line scan the mixing of Si and Ga was confirmed.

Figure 19b shows the integrated intensity of the Ga L2, 3 and Si K edges, which again shows a 1 nm wide region containing both Si and Ga. The data in Figure 19 demonstrate that there is significant disorder and mixing occurring at the diamond/SiN and SiN/GaN interfaces. The potential of SiC formation at the diamond/SiN interface may be helping in creating an ordered transition from the GaN to the diamond. SiN thin film thermal conductivity has been measured to be as low as 0.34 W/m-K for a strained 50nm thin film [28]. However, even with the low thermal conductivity of SiN, its ability to act as an etch barrier between the diamond growth environment and the GaN allows for a much smoother interface transition between the GaN and diamond, and the added resistance due to the SiN is less significant than the disorder displayed with both the sample G and A.
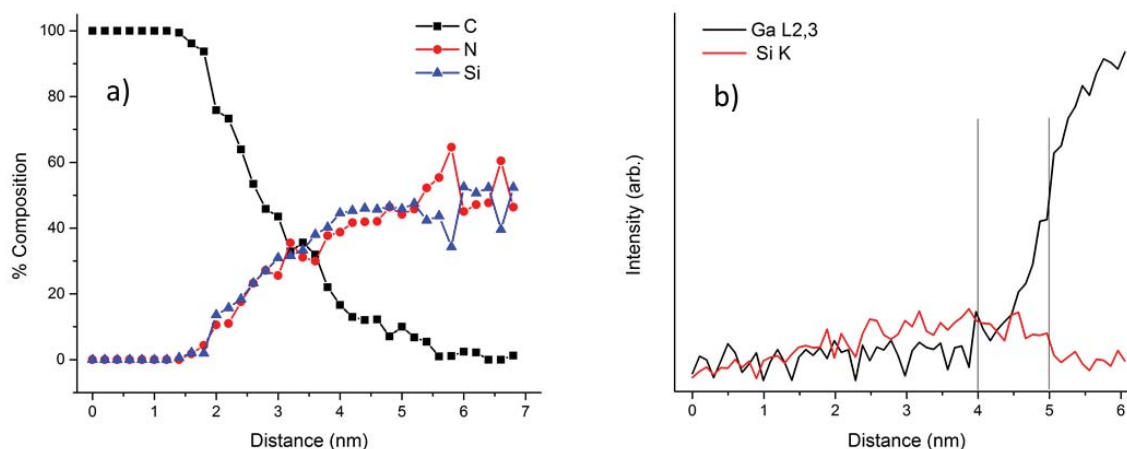
Figure 19: Chemical Composition of Interface

(a) Composition mapping of a line scan across the center of the HAADF image. The scan clearly demonstrates a gradual decrease in carbon moving through the interface. (b) Integrated intensity of Ga and Si for a line scan across the interface. Mixing of Si and Ga is observed in a 1 nm region as indicated by the vertical lines

In summary, this study used TDTR to measure the interfacial resistance of three different samples that contained diamond grown on directly onto a GaN layer. It is apparent that even with a relatively low thermal conductivity, SiN is the best choice of the three samples presented here for helping to facilitate the growth of diamond directly on GaN, and that due to the elevated temperatures and hydrogen rich environment, etching of the GaN during the growth must be considered. It was also found through HAADF imaging that a relatively smooth transition with intermixing of elements takes place throughout the interlayer, thereby reducing disorder and enhancing phonon transport across the interface.

Approved for public release; distribution is unlimited.

3.2   Improving Thermal Boundary Resistance Using Patterned Interfaces

While the large thermal conductivity of CVD diamond makes it an excellent candidate to cool high power electronics, the large lattice mismatch between diamond and other applicable materials (e.g. GaN, Si) leads to large thermal interface resistance at the heterointerface that impedes heat dissipation. Therefore, it is of great importance to reduce this thermal interface resistance. For this study, we used a patterned silicon substrate to grow diamond as shown in Figure 20. Compared with the flat silicon substrate, these patterned features work like "fins in convective heat transfer", which increase the effective heat exchange area and subsequently facilitate heat transfer across the interface. Additionally, the confinement of the trench walls forces the diamond crystals to grow at a preferred orientation (110), which further enhances thermal transport near the nucleation interface. Both factors contribute to decreasing the total thermal resistance across the film and diamond-silicon interface as a result of the substrate patterning prior to deposition.
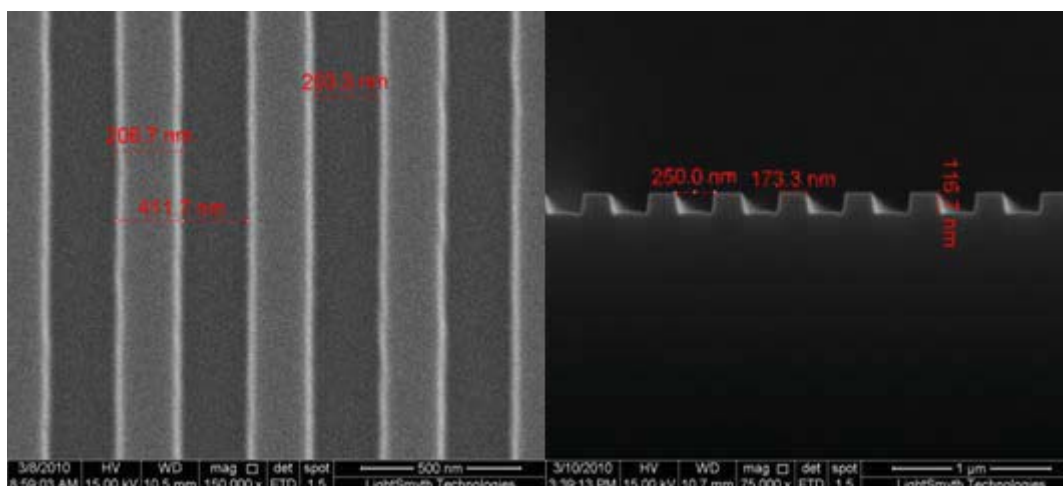
Figure 20: Geometry of Patterned Interface
Plan view (left) and cross-section (right) SEM images of a patterned silicon substrate prior to deposition of CVD diamond.

We measured three patterned interface samples with different pattern sizes and one flat sample as reference by TDTR. The parameters of the patterns are shown in Table 5. A layer of 2 um diamond was grown on the four substrates with the same grown conditions. Then 100 nm Al was coated on the diamond as transducer. The schematic diagram of the sample configuration is shown in Figure 21.
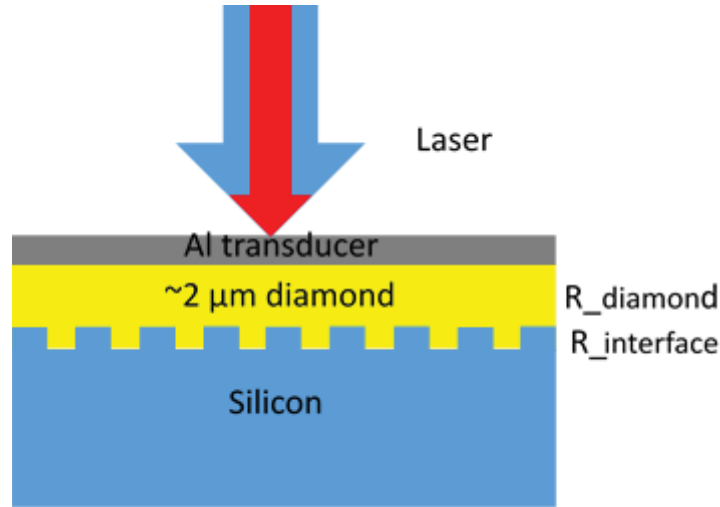
Figure 21: Samples for Measuring Patterned Interface
Schematic diagram of samples measured by TDTR.

TDTR was used to measure the total thermal resistance of the diamond layer and the diamond-silicon interface. We used multi-frequency measurements (1.2 MHz or 2.2 MHz and 3.6 MHz) to measure the Al-diamond interface conductance, cross-plane diamond thermal conductivity, and diamond-silicon interface conductance. Here, we fixed the in-plane thermal conductivity as 120 W/m-K according to other NRL 2 μm diamond membrane samples. The sensitivity of in-plane thermal conductivity of diamond is very small so the measurement error resulting from the in-plane thermal conductivity value is negligible. Because it is hard to separate diamond cross-plane thermal conductivity and the diamond-silicon interface conductance, we report the total resistance of the diamond layer and the diamond-silicon interface, as shown in Table 6.

Table 6. Parameters of the Si-Diamond Patterned Interface

Sample	Period (nm)	Groove Depth (nm)	Duty Cycle	Line Width (nm)	Relative contact area	R_total (m²-K/GW)
A	139	50	50%	69.5	**1.72**	**14.1**
B	416.6	110	50%	208	**1.53**	**17.0**
C	833.3	200	50%	416	**1.48**	**18.8**
Ref.	0	0	0	0	1	**22.1**

The total resistance decreases with decreasing period of patterns and decreases with increasing effective contact area. The enhanced thermal conductance across both the diamond film and the diamond-silicon patterned interface is due to a combination of two factors, the first being the enlarged effective contact area between diamond and silicon, and the second being an increase in the preferred (110) texture of diamond that leads to an increase in the thermal conductivity of the film itself. The former factor is analogous to the effect of maximizing the effective cooling area of a fin structure in a heat sink, providing a larger surface area for a given heat flux to pass

across when traveling from one material to another. We believe that the relative contact area between the two materials is the dominant effect that leads to the observed impact on the total thermal resistance of the diamond on patterned silicon structures when compared to the reference case based on the correlation between an increase in relative contact area resulting in a decrease in total resistance.
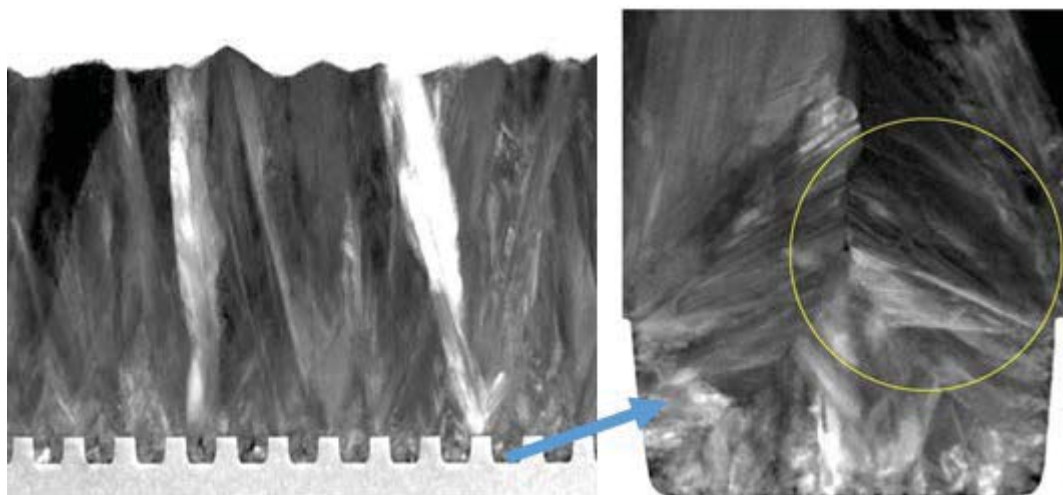
Figure 22: TEM of Diamond Growth on Interface Patterns
Cross-sectional TEM images CVD diamond deposited on a patterned silicon samples, highlighting the directionality of grain formation emanating from the bottom and sidewalls of the trenches.

However, in conjunction with the influence of relative contact area, there is an additional contribution to the reduction in the total resistance of the patterned samples compared to the reference case due to the observation of preferential crystallographic texturing within the CVD diamond thin film when grown on the patterned samples. The preferential orientation/texturing of the material has the potential to impact photonic thermal transport in a variety of ways, such as significant differences in phonon dispersion relations between various crystallographic directions that can influence both transport within, as well as across grain boundaries. By constraining the material to possess a single, preferred orientation, the impact of these scattering effects between grains with different orientations can be minimized, leading to improved phonon transport and higher thermal conductivities.

Figure 22 shows TEM cross-sectional images of a similar sample of CVD diamond (1 μm thick) grown on patterned substrate type 'A' (139 nm period, 50 nm groove depth) to illustrate certain features of the crystal morphology that results when growth is templated from these patterned structures. As seen in the images, the growth of the CVD diamond tends to progress in a direction normal to the surface that it nucleated from, often merging with other crystal growth "fronts" in a region above the trenches in the patterned silicon (right image in Figure 22). We refer to this merging of grain growth as "impingment" and note that these impinged regions tend to remain well defined in the cross-sectional images as growth continues.

Approved for public release; distribution is unlimited.

The creation of these impinged grains has a significant impact on the morphology of the resulting CVD diamond films, encouraging a preferred (110) growth orientation within the grains of the diamond compared to randomly-oriented grains in the reference case (no patterning). The degree of (110) texturing observed in the samples grown on patterned substrates was confirmed via analysis using two separate techniques; direct observation of the lateral growth of (110) oriented grains as a function of distance from the nucleation point via TEM imaging, as well as quantification of the texture coefficient of (110) versus (111)-oriented diamond using x-ray diffraction (XRD).
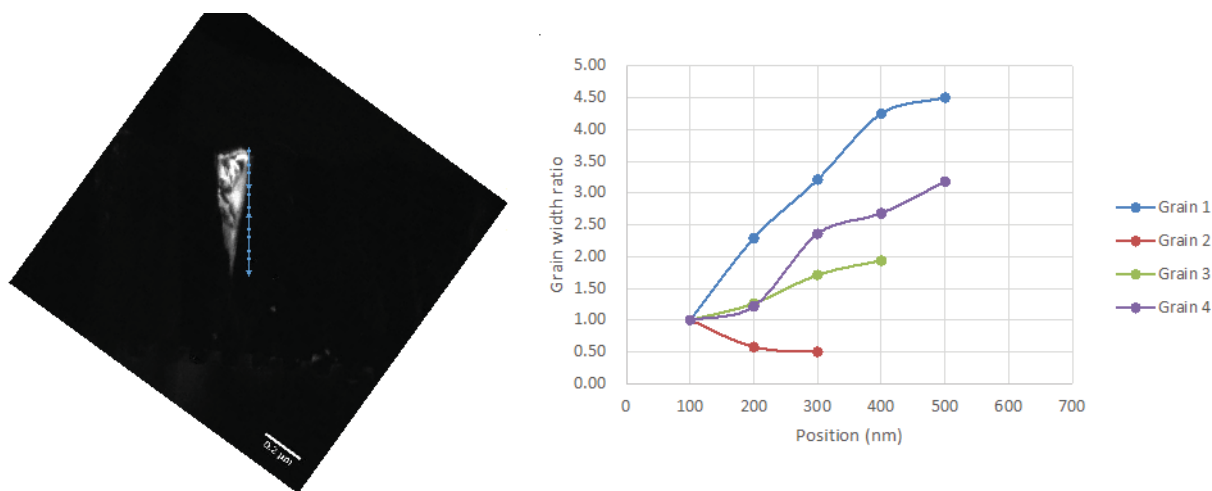
Figure 23: Grain Expansion during Growth

(Left) TEM cross-section image of a (110)-oriented grain, highlighting the fact that the lateral width of the grain tends to increases as the growth progresses from the nucleation side of the film (bottom) to the surface (top). The increase in lateral width indicates a preferential increase in volume-fraction of (110)-oriented material as the film is grown. (Right) Analysis of the grain width ratio for four different grains (grain #4 is the same as pictured in the TEM image at left), indicating that the increase in (110)-oriented material is apparent in multiple grains within the film.

Figure 23 depicts the results of the first technique where TEM cross-section images are used to quantify the increase in (110)-oriented diamond through changes in the lateral sizes of specific grains within the film. The image at left depicts a (110)-oriented grain within the CVD diamond film that can be used to assess the change in volume fraction of material with this orientation via the grain width ratio. The grain width ratio is defined as the width of a grain measured at some distance from a point 100 nm from the nucleation/patterned region divided (effectively normalized) by the width of the grain at that 100 nm point. The result is a parameter that can quantify how the lateral width of the grain in question changes as the growth of the film progresses beyond a chosen point from the nucleation point. The plot at right in Fig. 23 depicts the results of this analysis performed on four different (110)-oriented grains within the diamond films. In three of the four grains investigated, the grain width ratio increases with increasing position from the 100 nm normalization point, indicating that the lateral width of the grain is increasing as the film grows thicker. Given this increase in the lateral width of the (110)-oriented grains, the argument is that the volume fraction of (110)-oriented material is increasing overall as the diamond film grows when template on patterned silicon interfaces.
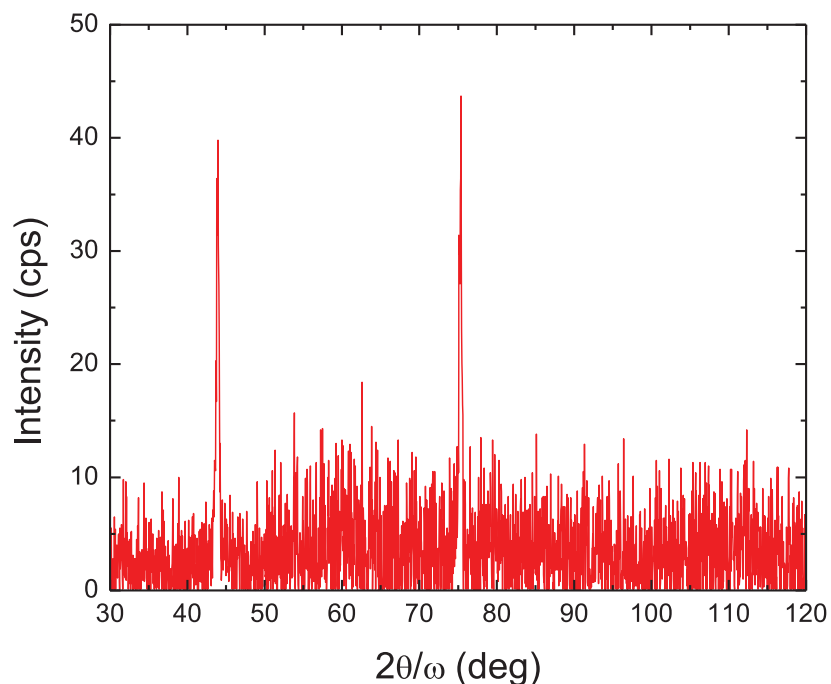
Figure 24: XRD Analysis of the Grain Texture
X-ray diffraction (XRD) scan of CVD diamond material grown on patterned silicon substrate type 'A'. (111) and (220) diamond peaks are observed in the XRD scans, indicating that this crystallographic orientations are present in the material being investigated. The inset is a table of the relative intensity of these same peaks in powder diamond to serve as a reference for assessing the degree of texturing in the films. These powder values as used along with the peak intensities measured for the films to calculate the texture coefficient, resulting in an assessment that the diamond films grown on patterned silicon exhibit stronger (110) texturing compared to (111) oriented material (three times larger).

In conjunction with this direct analysis of the local geometry of individual grains within the film, further evidence of preferential (110)-texturing in films grown on patterned substrates was obtained via XRD measurements. Figure 24 depicts an XRD scan of CVD diamond grown on patterned silicon substrate type 'A' where strong (111) and (220) diamond peaks are clearly present. In order to use these peak intensities to assess the degree of texturing present in our thin film samples, a calibration is required using powder diamond material to provide a baseline regarding the relative intensity between these same peaks in randomly-oriented material (hence the use of powder diffraction). The relative intensity between these same peaks in the case of powder material is shown in the inset of Figure 24. Using the peak intensity information from both the powder and thin film measurements, a texture coefficient can be calculated to quantify the relative amounts of material present with a particular preferential crystallographic orientation. Based on this analysis, it is determined that the texture coefficient of (110)-oriented material (determined using the (220) peaks) is a factor of three times larger than the coefficient of (111)-oriented material (1.56±0.03 versus 0.54±0.03, respectively). This result further confirms that the growth of CVD diamond on patterned substrates results in a preferred (110)-orientation of the grains.
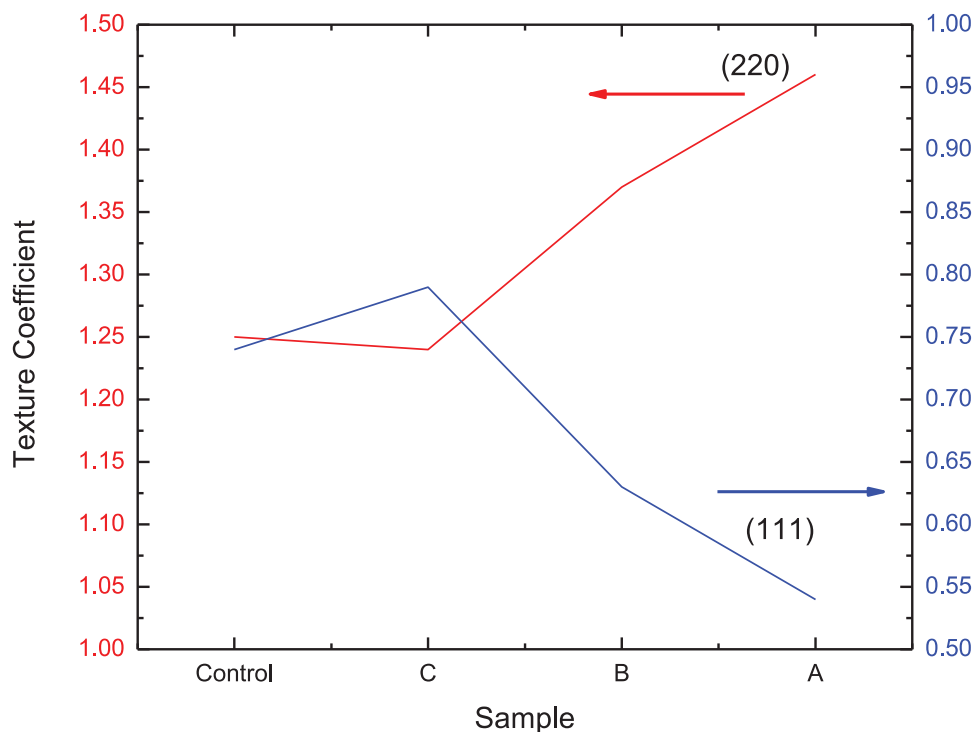
Figure 25: Texture Coefficient for Diamond Film

Texture coefficients for (111) and (110)-oriented material present in various CVD diamond thin films grown on both patterned (A,B,C) and unpatterned (control) substrates, determined via XRD (the geometry of each patterned sample is given in Table 6). As both the periodicity and depth of the grooves decreases (see Table 6), the amount of (110)-oriented CVD diamond material increases, as indicated by the increase in the (110) texture coefficient (and the commensurate decreased in the (111) coefficient.

Texture coefficients for both (111) and (110)-oriented material were collected in an identical fashion for each of the four samples studied (A, B, C, control) and the results are plotted in Figure 25. It is apparent from the plot that the largest degree of (110) texturing (and consequently the smallest degree of (111) texturing) is present in sample type 'A' which possesses the shortest period (139 nm) and shallowest grooves (50 nm) of the sample set. As both the period and groove depths increase from sample 'A' to sample 'B' and then increases further for sample 'C', the degree of (110) texturing present in the CVD diamond films decreases, eventually reaching the texture coefficient observed in the control film with no patterning. Based on these results, it appears that reducing the dimensions (periodicity and depth) of the patterned silicon structures encourages the CVD diamond grains to orient themselves so that they exhibit a larger degree of (110) texturing. This increase in (110) texturing observed in the diamond grown on the patterned silicon samples will also contribute to the observed reduction in the total resistance (given in Table 6) compared to the control sample through the improvement in the thermal conductivity of the diamond film itself.

4. Determination of Diamond Thermal Conductivity and Grain-To-Grain Thermal Resistance

The high thermal conductivity of diamond (up to 3300W/mK) has been widely exploited in thermal management of different applications, e.g. high power lasers, high power light emitting diodes (LEDs), x-ray optical windows and high power electronic devices. In all of these applications, and because nowadays polycrystalline diamond can reach thermal conductivities approaching those of single crystal diamond, polycrystalline rather than single crystalline diamond is used without any detriment.[29] However, for achieving this performance polycrystalline diamond needs to be polished removing the material of the first microns of growth corresponding to the near nucleation diamond.[30] In this region, comprising the first microns of diamond from nucleation, the thermal conductivity is much lower than bulk values; it is also anisotropic i.e. cross-plane and in-plane thermal conductivity differ in value; the thermal conductivity also shows a strong dependence on the average grain size.[30, 31] Due to the difficulty of measuring the thermal properties of ultra-thin diamond films, the thermal transport in this region of the diamond has been scarcely studied, and the existent data reported in the literature show significant disparity in values.[31] However, the recent integration of diamond with GaN high electron mobility transistors (HEMTs) has revived the interest in a better understanding of the diamond properties in this near-nucleation region, since a low thermal conductivity in this region may be a bottleneck for this technology. It should be noted that the thermal conductivity values reported in the literature for ultrathin diamond layers (<3µm) range from a few tens to few hundreds of W/mK, with cross plane/in-plane anisotropy rates ranging from 1.5 up to 20. [30-33] To explain these low thermal conductivity values, two main factors have typically been considered: the low quality of the diamond lattice in this region, and the presence of grain boundaries acting as thermal barriers. The latter has also been qualitatively used to justify the anisotropy in thermal conductivity due to the characteristic columnar shape of the polycrystalline diamond grains.[6,8] However, while these two factors undoubtedly impact the heat transport in the near nucleation diamond region, still it is poorly understood how to quantify their individual contribution to the reduction of thermal conductivity and how they are related to the emergence of anisotropy in the heat conduction. The quality of the lattice in polycrystalline diamond is typically explored by means of its Raman signal. When approaching the near nucleation diamond it is common to observe features attributed to a low-quality lattice: the sp^3 diamond peak becomes broader than for single crystal/bulk CVD diamond, and other features appear in the Raman spectrum apart of the diamond Raman peak (sp^2 bonds, transpolyacetylene peaks, etc.). However, while this is clear evidence for a somewhat less crystalline lattice structure, it says little about whether these contributions to the Raman spectra arise from the in-grain lattice or from the grain boundaries regions, which are prone to accumulate defects including sp^2 and CH_x bonds. On the other hand, theoretical values computed from molecular dynamics simulations have shown that the thermal resistance between perfect grain boundaries in polycrystalline diamond range between 0.02-0.1 m^2K/GW depending on its mismatch angle. However, reported literature values from experimental measurements are much higher, on the order of 0.5-3 m^2K/GW, which can only be explained by a significant accumulation of defects/disorder at and near the grain boundaries. It is worth noting that experimental values of grain/grain thermal resistance are typically extracted indirectly from experimental data. For this, models make use of strong simplifications, for example, bulk-like in-grain thermal conductivities and a single average value for the in-plane grain size (in the case of

Approved for public release; distribution is unlimited.

the columnar grains those may be somewhat arbitrary due to the lack of regularity) are considered. In any case, how the grain/grain thermal resistance correlates with the cross-plane thermal conductivity, and therefore the thermal conductivity anisotropy factor, is still poorly understood, and at best only approached by simplified models making use of indirect phenomenological relations. To shed some light on this problem, we demonstrate in this work a methodology able to unravel the individual roles of grain boundaries and lattice thermal conductivity on the thermal transport in the near nucleation site of polycrystalline diamond. For this, we have determined the in-plane and cross-plane thermal conductivity experimentally in a polycrystalline diamond thin film (1µm thick). This has been combined with thermal simulations making use of the real grain structure, including grain orientation, of the sample, which was determined by TEM. Using this methodology the in grain thermal conductivity and thermal resistance between grains can be simultaneously determined from both cross-plane and in-plane measurements without any fitting parameters.

4.1   Experimental Details

Diamond films of about 1 µm thickness were deposited on 200 µm thick silicon substrates by microwave plasma-assisted chemical vapor deposition (MPCVD) in an IPLAS 5.0 KW CVD reactor with hydrogen and methane as reactant gases. The substrate temperature and chamber pressure were kept constant throughout the entire diamond film growth and remained at 750°C and 7.08 torr respectively. The microwave power and methane to hydrogen ratio was varied, respectively, from 800 W and 0.5% during the initial 20 minutes of film growth to 1400 W and 0.7% through the continuing diamond deposition. The diamond film thickness was measured by in situ laser reflectometry. Prior to growth, the silicon substrate was seeded by ultrasonic treatment in ethanol-based nanodiamond suspension prepared from detonation nanodiamond powder which was acquired from International Technology Center (ITC), North Carolina, USA. According to the manufacturer specifications the material grade used here has a high degree of grain size homogeneity with an average particle size of 4 nm, and a chemical purity in excess of 98%. SEM analysis of the back side of a typical diamond film deposited with above mentioned seeding method shows a uniform nucleation with seed density greater than 10^{12} nuclei/cm^2. In general, the use of carbon-lean growth conditions is intended to suppress secondary renucleation, and increases film quality by decreasing grain/boundary ratio. Such diamond films are basically formed through the grain coalescence and subsequent growth competition of initially random oriented nanodiamond seeds. The orientation of crystallites fastest growth direction in relation to substrate surface is the key to seeds survival. Only the crystallites with fastest growth direction nearest to normal to the growth surface survive at the end. This ultimately leads to a formation of a well pronounced columnar grain structure in the film, as well as an increase in lateral grain size with film thickness.

The structural characterization included electron microscopy x-ray scattering techniques. Electron transparent plan view and cross section samples were prepared using a focused ion beam (FIB) instrument (Nova 600 FIB). SEM images of the diamond surface morphology were also produced using the FIB instrument. Transmission electron microscopy (TEM) images were generated using a Titan S/TEM (FEI) system under 200 kV. The scanning transmission electron microscopy (STEM) mode allows to analyze the grain size distribution while the high angle annular dark field (HAADF) detector in the STEM mode provides contrast based on the differences in the adjacent grain orientation and distinguishes clearly between grain boundaries

and twins (Figure 26). The orientation of the different grains was quantified using two techniques. First, selected area electron diffraction (SAED) patterns were used to produce images of grains with specific orientations. Tilting the sample imaged different grains, so the relative misorientation between adjacent grains could be estimated. The second approach was to employ precession electron diffraction (PED) mapping with a 10 nm step size from which the orientation of each grain is mapped using a color-coded legend. X-ray scattering measurements utilized a Jordan Valley D1 (Cu Kα radiation) with incident parallel beam optics for both 2θ:ω scans and pole figures using Soller slits. Full pole figure data were collected with a fixed diffraction angle 2θ by varying the tilt angle with respect to the sample surface normal direction (χ) from 0° to 80° with a step size of 2° and rotation angle around sample surface normal direction (φ) from 0° to 360° with a step size of 1°. Pole figures were plotted with the obtained diffracted intensity data as a function of χ and φ.

For producing diamond membranes for in-plane thermal measurements, the silicon substrate was etched away by dry etching to obtain several 460x1000 µm freestanding diamond membranes as shown in Figure 27. Test structure designs consisted of metal heaters on these diamond membranes; this generates a temperature field in the freestanding diamond membrane when an electric current flows through the line heater. The test structures were fabricated by first patterning 20 nm Cr followed by 300 nm Au by lift-off lithography. Diamond etching was performed by first depositing SiN by plasma-enhanced chemical vapor deposition (PECVD) and patterning by inductively coupled plasma (ICP) reactive ion etch (RIE) using SF_6. Diamond was etched by RIE ICP O_2/Ar_2 chemistry. The SiN mask was removed by a combination of RIE ICP and buffered HF. Diamond membranes were fabricated by Bosch etching of the Si wafer to produce deep vias stopping selectively on the diamond film.
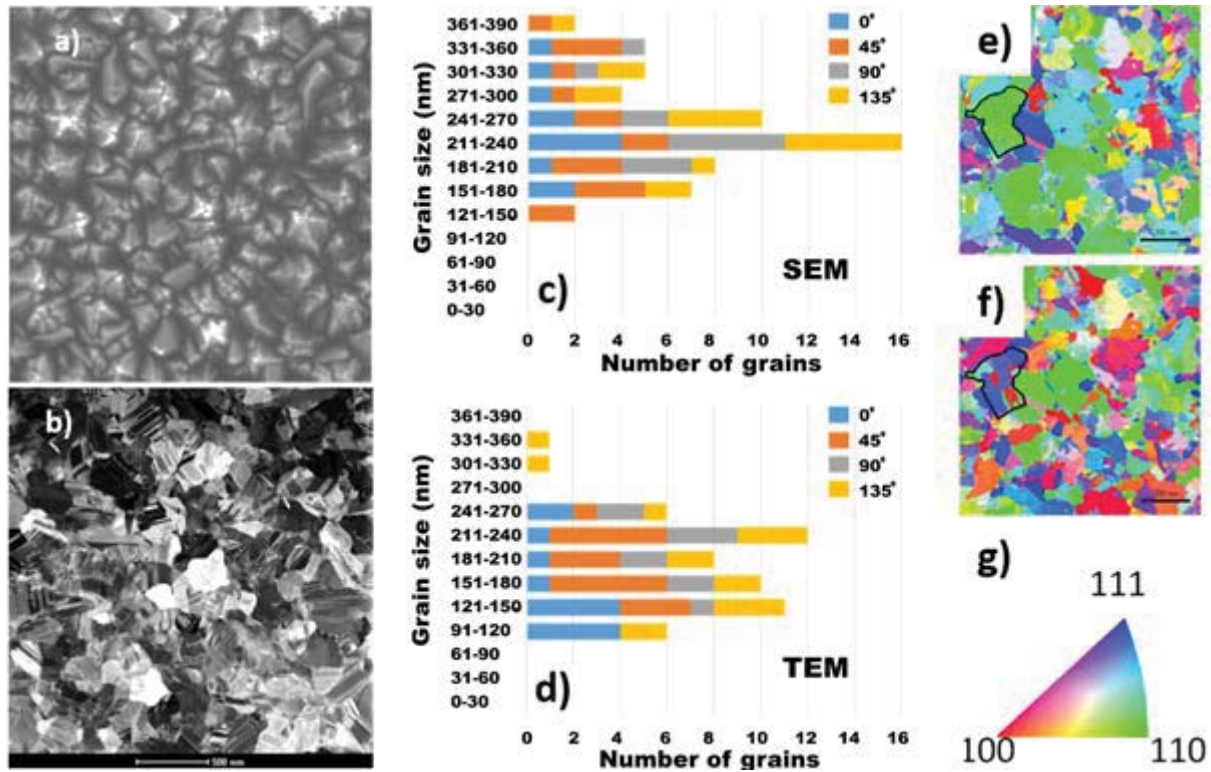
Figure 26: Analysis of Grain Size Distribution
(a) Plan view image of the measured diamond layer surface using SEM, and (b) from a STEM image extracted from the surface region of the diamond film. The scale bar shown in (b) is also the scale bar for (a). (c) Distribution of the grain dimension from the SEM image and (d) from TEM. (e,f) correspond to PED orientation maps with (g) providing the orientation legend.

4.2   Experimental Measurement of the Diamond Microstructure

The in-plane grain size distribution, both using SEM and TEM, was determined using the standard intercept method with four directions (0°, 45°, 90° and 135°) chosen to account for the non-equiaxed grains, as shown in Figure 26. The average grain size obtained is 184 nm from the TEM plan view image (Figure 26a), and 240 nm from the SEM image (Figure 26b). It can be seen that the TEM image shows better contrast between different grains, and therefore displays the actual grain boundaries. On the other hand, in the SEM image, small grains without significant contrast difference do not show visible grain boundaries, and are typically regarded as part of another grain. The difference is demonstrated in the grain size distribution plots: the distribution using the SEM image (Figure 26c) shows larger grains with greater than 300 nm size, whereas the distribution determined from the TEM image (Figure 26d) shows a smaller average grain size and the presence of grains less than 120 nm in size. A more accurate determination of the grain distribution (using TEM) provides important input into the thermal analysis. Therefore, TEM approach will produce a more accurate grain size, while the SEM approach is more likely to overestimate the grain size. Figure 26e and Figure 26f correspond to PED orientation maps, the out-of-plane and in-plane orientation of each grain, respectively. Qualitatively, there are more grains with an out-of-plane orientation closer to (110) than other orientations, suggesting that the growth parameters favor a preferred out-of-plane (110)

orientation. A comparison of the out-of-plane and in-plane orientations provides further insight into the grain orientations and sizes. At the left center of Figure 26e and Figure 26f is a region delineated by a thick black line. The out-of-plane image (Figure 26e) indicates that this region has (110) orientation but the in-plane image (Figure 26f) shows that this region is actually comprised of an agglomeration of smaller grains with different in-plane orientation.

Figure 27 shows the (220) and (111) pole figures of the diamond film. The x-ray beam illuminates a surface area of several mm^2 and therefore provides a better overall average of the film properties compared to the TEM measurements which includes a small number of grains. Note that a pole figure with a uniform color would indicate a random orientation of grains. Confirming the earlier results, Figure 27-a shows that there is a preferred orientation of (110) grains (using the (220) reflection) oriented in the out-of-plane direction – corresponding to the central region of the figure. The (111) pole figure (Figure 27b), on the other hand, shows a reduced intensity in the center region and a ring of stronger intensity at ~ 35° from the central region. The (111) reflected intensity at this angle corresponds to those grains that have (110) planes parallel to the surface (the angle between (111) and (110) for a cubic crystal is 35.3° or 90°). This 'ring' of intensity is also relatively uniform in intensity, indicating that the in-plane orientations of the diamond grains are random.
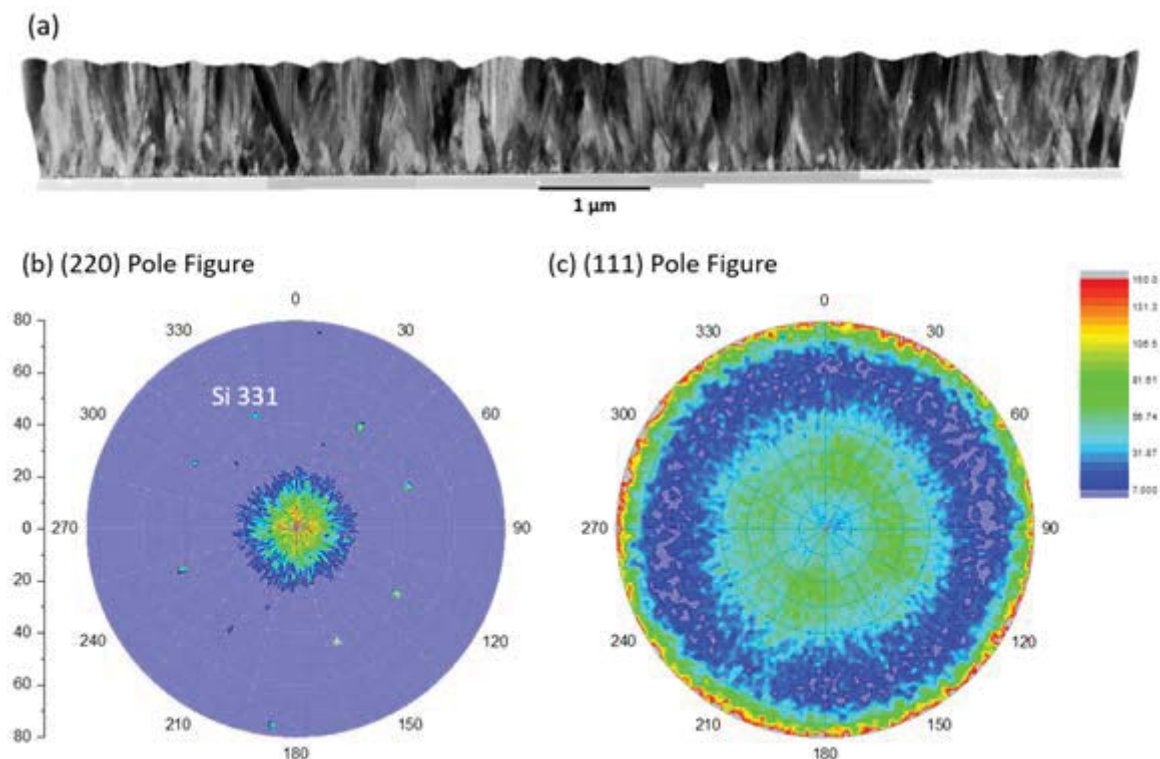
Figure 27: Pole Figures of Grain Orientation for CVD Diamond Film
(a) Transversal TEM image showing the grains and stacking faults/twins in the diamond film studied. (b,c) pole figures showing preferential (110) orientation of the grains. Note also there are also eight points of intensity at 46.5° from the center. These correspond to the (331) planes from the Si substrate. The Bragg angle for the (331) Si reflection is within 0.5° of the diamond (220) so it is also captured in this measurement.

The cross-section grain structure of the diamond film is shown by the STEM image in Figure 27a. The different grain orientations are observed through the gray-scale contrast and the elongated nature of the grains is evident. Twins are typically observed as straight-line boundaries of one contrast within a region of different contrast, as labeled in the figure. Also, near the silicon interface, the nucleation region is clearly observed by the presence of several nanoscale grains. The STEM image does provide a useful reference for the grain growth, presence of grain boundaries and twin boundaries, but the actual boundaries are delineated using a series of images from SAED patterns and from PED measurements.

4.3   Experimental Measurement of the Thermal Conductivity: Raman and TDTR

To determine thermal conductivity, temperatures are measured at specific points in the diamond membranes by Raman thermography assisted by nanosensors to minimize errors. For this, a variation of the technique consisting of using of TiO_2 nanoparticles with a purity of 99.98% (Anatase) and with an average size of 30 nm were sonicated in ethanol and deposited onto the sample by drop casting, keeping the sample above the ethanol boiling point to achieve a homogenous deposition on the sample. TiO_2 nanoparticles were selected as Raman nanosensors since they have a very strong Raman cross-section, high sensitivity to the temperature when using the E_g 143 cm^{-1} Raman peak and negligible phonon confinement effects above 20 nm nanoparticle size. The Raman shift induced by the temperature field in the diamond membranes and TiO_2 nanoparticles was acquired using a Renishaw InVia spectrometer making use of a 488 nm laser beam focused by a 50× (0.65NA) objective. The response to a temperature change of the E_g 143cm^{-1} Raman shift was calibrated in a Linkam thermal stage for several nanoparticles. A 4-probe configuration was used to accurately monitor the electrical power dissipated in line heaters on the freestanding membranes; the thermal conductivity of the film was extracted by comparing the experimental temperature measurements with a finite element solution of the temperature field in the membrane. Temperature profiles obtained across one of these freestanding membranes for two different powers together with the simultaneous fit from the finite element thermal simulation are shown in Figure 28a. Besides, the peak temperature in the center of the membrane versus the power dissipated in the heater is shown in Figure 28b. This was measured through Raman thermography on a TiO_2 nanoparticle in the middle of the heater and additionally by monitoring the change in the resistance of the line heater with the temperature of the central part of the heater (see Figure 28b, inset). The perfect linear behavior observed in Figure 28b clearly shows that the thermal resistance of the diamond film does not change significantly in the 20-200°C temperature range, and thus neither does its in-plane thermal conductivity. It should be noted that electrical measurements above 150°C were not reliable, most likely due the intermixing of Au with the thin layer of Ti used as adhesion layer used for their fabrication; however, in the 25-150°C range, an excellent agreement between the two methods was observed. Finally, the above-described measurements were repeated in more than 10 membranes distributed along the entire wafer, and an average value of 95±10 W/mK was extracted for the in-plane thermal conductivity of this material. This value, while much lower than the one found in single crystal diamond, is in line with what has been previously measured in our program.
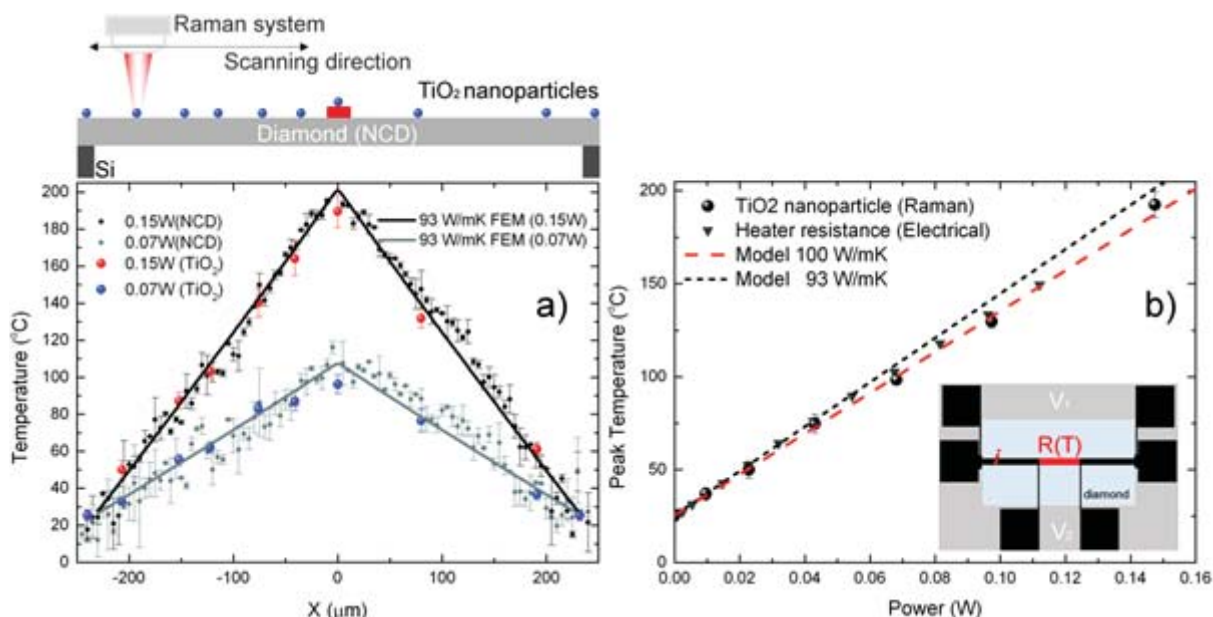
Figure 28: Raman Measurement of NCD Diamond Film

Example of the in-plane thermal conductivity measurements performed on the measured diamond membrane. (a) Temperature profiles obtained from the diamond and TiO₂ nanoparticles on the freestanding diamond membrane (see sketch, top) for two different powers and its simultaneous fitting with 93 W/mK. (b) Temperature in the central region of the membrane (red area in inset illustrating sketch of heater and contact layout) vs power dissipated in the heater measured on TiO₂ nanoparticles and by electrical thermometry

The through-plane thermal conductivity of the diamond film is measured using TDTR. A standard samples configuration for thin film thermal conductivity measurements by TDTR was used; the sample consisted of 90 nm of Al deposited on top of the diamond film on the Si substrate. The heating frequencies of 1-12 MHz fully penetrate the diamond layer so the measurement is also sensitive to the Si properties and the Si-diamond thermal boundary resistance. The three unknown parameters are the diamond through-plane thermal conductivity (κ_{dia}), the Al-diamond thermal boundary resistance (TBR_{Al-dia}), and the diamond-Si thermal boundary resistance (TBR_{dia-Si}). We define the average sensitivity for a TDTR measurement as given in equation 5. The average sensitivity provides a single sensitivity value for the entire time region of measurement to allow direct comparison of the ability to resolve different unknown parameters with the measurement. Figure 29a shows the average sensitivity to the three unknown parameters in the measurement; the sensitivity to the thermal conductivity of the diamond layer is lower than that of the two interfaces because the diamond layer is relatively thin (~1 µm) and conductive (>150 W/m-K). We simultaneously fit for the three unknown parameters using four different frequencies (Figure 29b). The uncertainties were calculated using a Monte Carlo simulation and the resulting diamond thermal conductivity was 175 +65/-42 W/m-K.
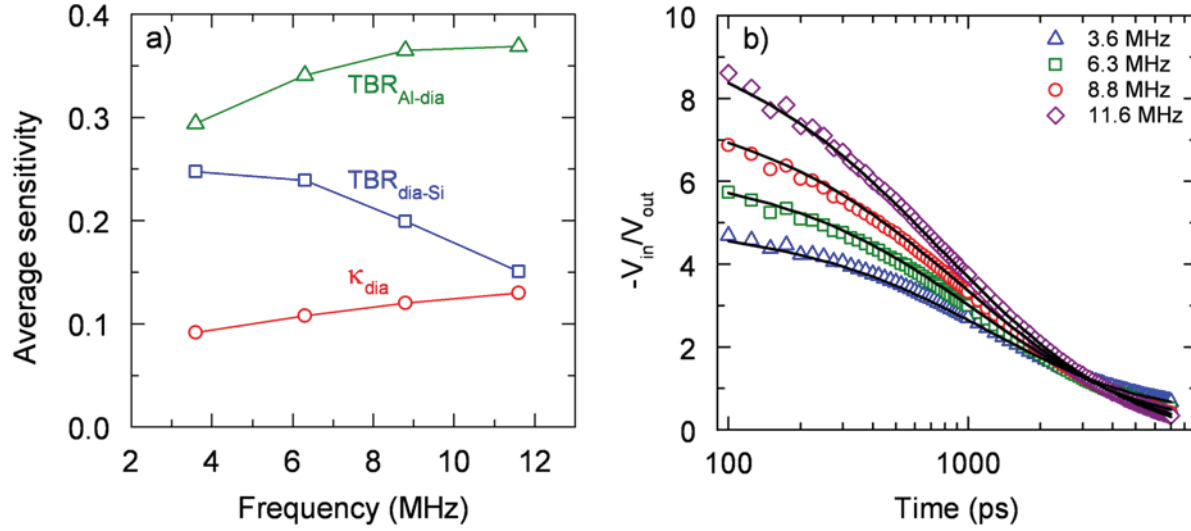
Figure 29: Sensitivity and TDTR Response for Measurement of Diamond Film
TDTR measurements: (a) Average sensitivity versus heating frequency for three unknown parameters: Diamond through-plane thermal conductivity (κ_{dia}), Al-diamond thermal boundary resistance (TBR_{Al-dia}), and diamond-Si thermal boundary resistance (TBR_{dia-Si}). (b) Four-frequency fit for three unknown parameters on N3S-200-070815, κ_{dia} = 175 +/- +65/-42, TBR_{dia-Si} = 13.7 +3.8/-3.5 m²-K/GW, TBR_{Al-dia} = 5.6 +0.6/-0.5 m²-K/GW.

4.4 Modeling and Data Analysis

To analyze the thermal transport in this kind of diamond material typically the in-grain thermal conductivity (lattice thermal conductivity) of the grains and the quality of the grain boundaries needs to be considered. This is typically approached by the following well-known relationship

$$\kappa = \frac{\kappa_{in-grain}}{1 + \frac{\kappa_{in-grain}}{d/R_{GB}}} \qquad (6)$$

with $\kappa_{in-grain}$ thermal conductivity of the grain lattice, d is the average grain size, and R_{GB} is the thermal resistance between grains. This formalism has proven to be a good description when grains are regular in shape and the mean free path of the phonons in the lattice is smaller than the distance between grain boundaries. However polycrystalline diamond shows a large disparity in grains sizes and also anisotropy in its geometry (see Figures 26-27). Therefore determining a unique average value for d in the cross-plane and in-plane directions is somewhat arbitrary for this material and also may depend on the technique, SEM or TEM, used to unravel the structure. Besides in diamond, a great amount of heat is carried by long mean free path (MFP) phonons, which may result in a lower $\kappa_{in-grain}$ than the one found in single crystals when the crystallites are smaller than 1 μm. Hence the three parameters appearing in Eq. 6, namely $\kappa_{in-grain}$, d, and R_{GB} must be determined from experimental data. Additionally, to explain with Eq. 6 the anisotropy observed from the in-plane and cross-plane measurements in an isotropic lattice, different values for d are needed. As a result an infinite number of combinations of $\kappa_{in-grain}$, d, and R_{GB} may reproduce and experimentally determined thermal conductivity, and therefore little information

can be obtained about the individual contribution of $\kappa_{in-grain}$ and R_{GB} to the thermal resistance of the material from Eq. 6.
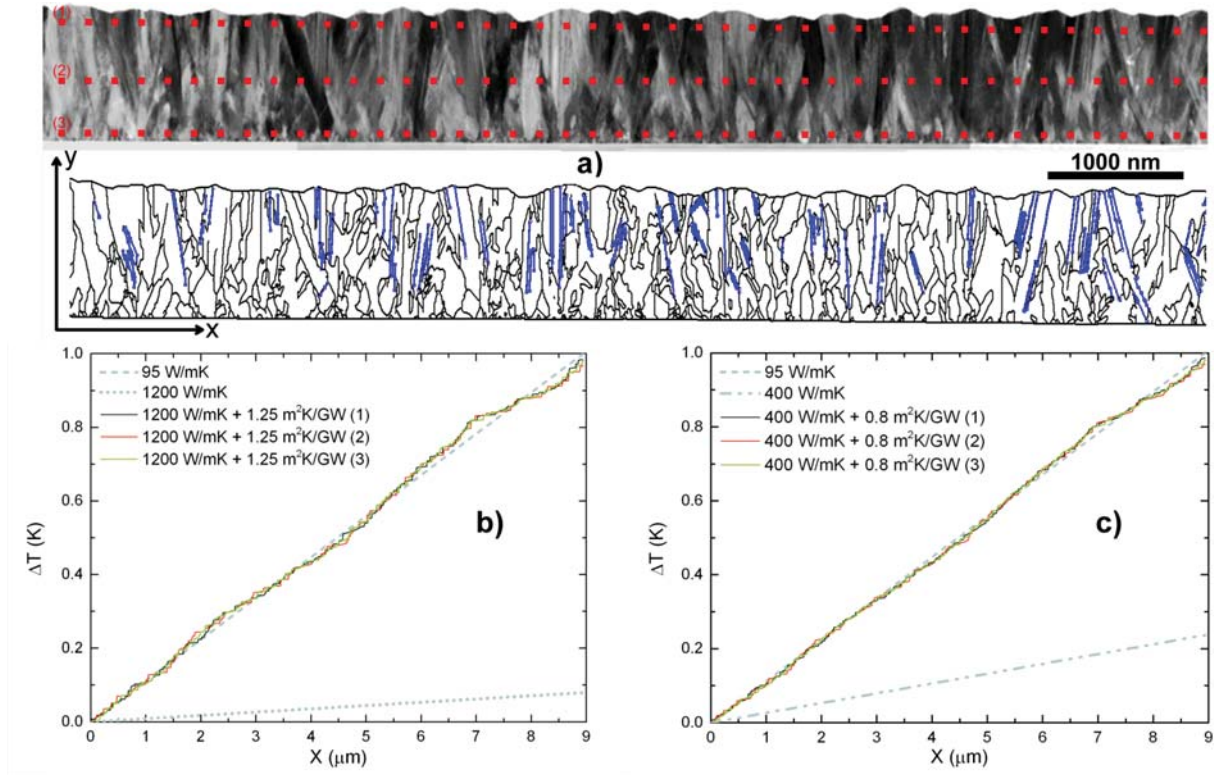

Figure 30: Grain Structure and Temperature Distribution across Diamond Film
(a) Grain structure of the film as determined from the TEM analysis. The twins detected in the film are remarked in blue. (b,c) Results of solving the in-plane heat equation, Eq. 7, in this structure along the film a slab with no grain boundaries and when grain boundaries are considered for a lattice thermal conductivity of 1200 W/mK and 400 W/mK, respectively. Note that a material with 95 W/mK can be reproduced with different combinations of $\kappa_{in-grain}$ and R_{GB}.

Here a different approach consisting of replicating the experiments by solving the heat equation on a long slab of material containing its real 2D grain structure, determined from the more accurate TEM technique, was used, thus removing the incertitude introduced by the average grain size. Since the material is relatively homogeneous in the growth plane (see Figure 26), we can approximate the experimental values measured in the films by the in-plane and cross-plane k_{eff} values of the 2D slab, and thus, only $k_{in-grain}$ and R_{GB} remain unknown. For this, the grain structure on a long slab of material of the diamond film determined by TEM (9 μm, see Figure 27a / Figure 30a) was incorporated into a thermal model implemented in COMSOL Multiphysics. The resulting geometry consists of more than 1000 grains of different shapes and sizes, containing more than 7500 boundaries in which the heat equation corresponding to an equivalent Raman (in-plane) and TDTR (cross-plane) thermal conductivity measurement experiments was solved. It should be noted that the magnitude of R_{GB} may depend on the orientation of the grains and the amount of defects that the boundaries accumulate. However, since the grains are preferentially oriented (see Figure 27), the effect of different orientations in

R_{GB} can be neglected here in first approximation. On the other hand, while grain boundaries are prone to accumulate defects, increasing their thermal resistance, twins/stacking faults provide cleaner boundaries. Therefore we considered here different boundary conditions for real grain boundaries and for twins/stacking faults which at best can reach, following molecular dynamics simulations, thermal resistances of 0.06 m²K/GW.

To reproduce theoretically an equivalent steady state experiment as the one used experimentally for in-plane thermal conductivity measurements, a prescribed heat density was imposed as a boundary condition in one of the ends of the slab, while a fixed temperature was imposed into the other end. For this condition, the thermal conductivity (k_{eff}) of a homogenous slab of material without interior boundaries can be easily determined from $q_0 = k_{eff} \times \Delta T / L$, where ΔT is the temperature difference between the heat source (q_0) and heat sink, and L is the separation between them. However, when the internal boundary conditions are considered the heat equation needs to be solved by finite elements subject to the following boundary conditions:

$$-\nabla g(\kappa(x,y)\nabla T(x,y)) = 0$$
$$-n \cdot q = q_0 \quad \text{for } x = 0$$
$$T = 20^\circ C \quad \text{for } x = L \tag{7}$$
$$\begin{cases} -n_L \cdot q_L = -\dfrac{(T_R - T_L)}{R_{GB}}, -n_R \cdot q_R = -\dfrac{(T_L - T_R)}{R_{GB}} \text{for grain boundaries} \\ \\ -n_L \cdot q_L = -\dfrac{(T_R - T_L)}{R_{twin}}, -n_R \cdot q_R = -\dfrac{(T_L - T_R)}{R_{twin}} \text{for twins} \end{cases}$$
$$-n \cdot q = 0 \quad \text{elsewhere}$$

If no thermal resistance between grains is considered Eq. 7 gives the trivial solution in which $k_{eff} = k_{in-grain}$; when the boundary condition for grain boundaries and twins in Eq. 7 is applied, then the value of k_{eff} is reduced from $k_{in-grain}$ as R_{GB} increases (see Figure 30). However, even having removed the incertitude introduced by the grain sizes, the experimental thermal conductivity can be reproduced with an infinite set of ($k_{in-grain}, R_{GB}$) values. We illustrated this behavior in Figure 30-b and 30-c, for two examples of these simulations using two values of $k_{in-grain}$, 1200 W/mK and 400 W/mK. To further reduce incertitude, and since these two parameters, $k_{in-grain}$ and $R_{boundary}$ are independent of the heat flow direction, we exploited the anisotropy detected experimentally to uniquely determine their value from simultaneously satisfying the in-plane thermal conductivity and cross-plane data in the 2D slab.
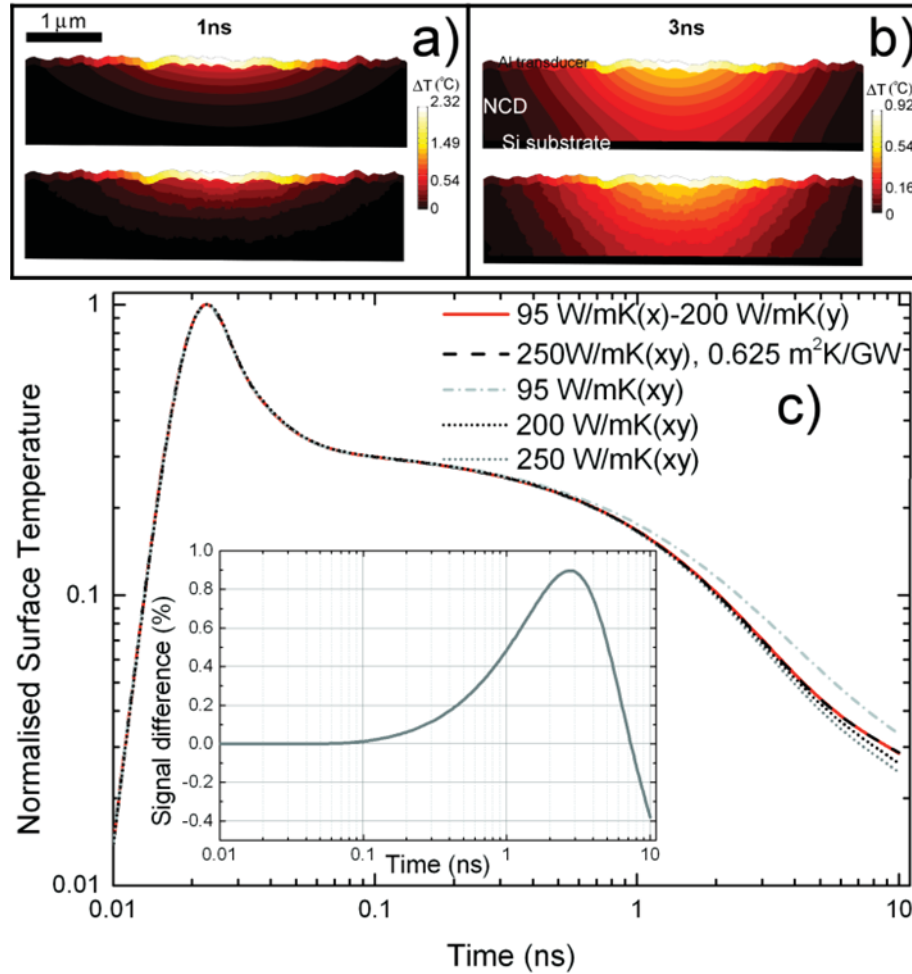
Figure 31: Model of Heat Spreading Under Transient Pulse in CVD Diamond Film
(a,b) Penetration of the heat wave applied to the top of the diamond film (with a Si substrate underneath the film) in an anisotropic 2D slab without internal boundaries (top), and in a slab with isotropic thermal conductivity of individual grains with internal boundaries (bottom) at different times. (c) Transient average temperature of the transducer surface as used in a TDTR experiment for various diamond thermal conductivities. Note that an anisotropic thermal conductivity and a material with a homogeneous thermal conductivity and internal boundaries have the same temperature transient signal. Inset, signal difference between the anisotropic material and its equivalent isotropic material with grain boundaries.

To reproduce an experiment similar to the one used for determining the cross-plane thermal conductivity, we created a transient simulation in the 2D slab containing the real grain structure of the film. For this, a homogeneous 100 nm thick layer was digitally added on top of the 2D slab to consider the Al transducer used in the TDTR experiments, and also a thick slab was added to the bottom of the geometry to take into account the Si substrate (see Figure 31-top). The thermal resistance between these two layers and the diamond was included as boundary condition into the thermal model which was solved by finite elements subject to the following boundary conditions:

$$\rho c_p \frac{\partial T}{\partial t} - \nabla g(\kappa(x,y)\nabla T(x,y)) = 0$$

$$-n \cdot q = q_0 \times \exp\left(-\frac{(\text{x-x}_0)^2}{\sigma_x^2}\right) \times \exp\left(-\frac{(\text{t-t}_0)^2}{\sigma_t^2}\right) \text{ for } y = \text{top Al surface}$$

$$T = 20\,^oC \text{ for } y = \text{ bottom Si surface}$$

$$\begin{cases} -n_U \cdot q_U = -\dfrac{(T_U - T_D)}{R_{Al-Diamond}}, -n_D \cdot q_D = -\dfrac{(T_U - T_D)}{R_{Al-Diamond}} \text{ for Al/Diamond interface} \\[2mm] -n_U \cdot q_U = -\dfrac{(T_U - T_D)}{R_{Diamond-Si}}, -n_D \cdot q_D = -\dfrac{(T_U - T_D)}{R_{Diamond-Si}} \text{ for Diamond/Si interface} \\[2mm] -n_L \cdot q_L = -\dfrac{(T_R - T_L)}{R_{GB}}, -n_R \cdot q_R = -\dfrac{(T_L - T_R)}{R_{GB}} \text{ for grain boundaries} \\[2mm] -n_L \cdot q_L = -\dfrac{(T_R - T_L)}{R_{twin}}, -n_R \cdot q_R = -\dfrac{(T_L - T_R)}{R_{twin}} \text{ for twins} \end{cases}$$

$$-n \cdot q = 0 \quad \text{elsewhere}$$

(8)

Here the first boundary condition (second line in Eq. 8) corresponds to the heat source, which is assumed Gaussian in both time and space. To simplify the simulation, a single pulse of 8 fs and a FWHM of 2 μm in size was simulated, keeping q_0 low enough to produce a temperature excursion in the diamond of less than 1°C. This enabled to linearize the problem by neglecting the temperature dependence of the thermal properties of the different materials (see Table 7).

Table 7. Thermal Properties used in the Transient Simulations

	ρ(Kg/m^3)	c_p (J/Kg□)	κ(W/mK)
Al	2700	897	175
Si	2330	705	148
Diamond	3515	490	X

In this simulation, the temperature on the surface of the Al layer was averaged according to the Gaussian distribution of the heat source, and an example of its output is shown in Figure 31 for different thermal conductivities and interior boundary conditions of the diamond layer. Note that in this simplified one-pulse simulation the first ~0.5 ns of the heat wave are almost independent of the properties of the diamond layer; however when considering a trail of pulses, like in the TDTR experiment, the thermal conductivity of the diamond may impact the composed heat wave earlier making the experiment even more sensitive to the cross-plane thermal conductivity than the simplified model. From 0.5 ns to ~4 ns the transient temperature of an anisotropic layer is almost indistinguishable from an isotropic material having a thermal conductivity equal to its cross-plane thermal conductivity; therefore, the heat wave is completely dominated by the cross-plane thermal conductivity. We want to note that the real size of the laser spot used in the experiment is bigger, and it will result in an even more dominant behavior of the diamond cross-plane thermal conductivity in this region. From 4 ns onward (eve later for bigger spot sizes) the in-plane thermal conductivity begins to dominate the heat propagation in the material, and thus it is not interesting. Besides, similarly to what we observed in the in-plane experiment, the transient profiles corresponding to an anisotropic material can be perfectly reproduced by a

material with a higher lattice thermal conductivity ($k_{in-grain}$) but with a thermal resistance between grain boundaries (see Figure 6, bottom and inset). Finally, we calculated the apparent cross-plane thermal conductivity by fitting the model with internal boundaries with a model without grain boundaries, and as a function of the thermal resistance between grains and for different in-grain thermal conductivities. These results are shown in Figure 32 together with those obtained in the in-plane simulations.
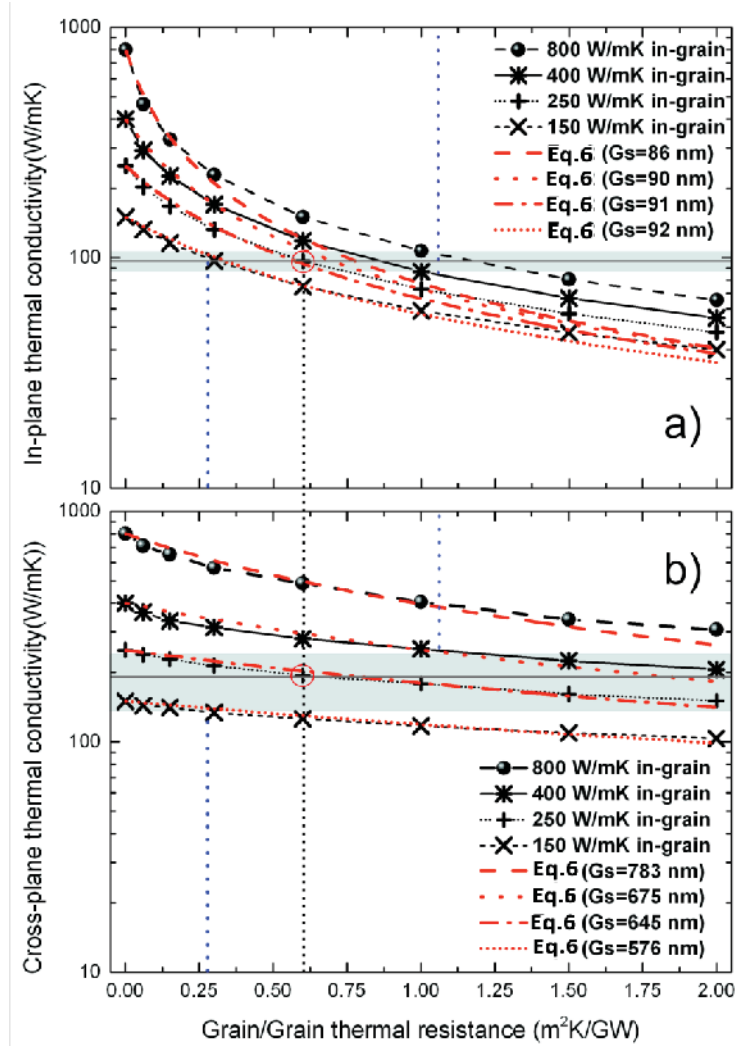
Figure 32: Analysis of Anisotropic Thermal Conductivity

Efficient in-plane (a) and cross-plane (b) thermal conductivity of the 2D slab of diamond shown in Figure 30 as a function of the grain boundary thermal resistance for different values of the lattice thermal conductivity. The horizontal grey band represents the experimental values including their error band. The simultaneous intersection of the theoretical curves with the average experimental values yields an in-grain thermal conductivity of 250 W/mK and a thermal resistance of 0.625 m²K/GW (black dotted line). Blue dotted lines allow to estimate the incertitude of these values. The best fits of Eq. 6 to the results obtained for the 2D slab containing the real grain structure are also shown in the graphs (red curves).

Approved for public release; distribution is unlimited.

As expected from the columnar shape of the grains, the in-plane thermal conductivity of the diamond film is more sensitive to the thermal resistance between grains than the cross-plane thermal conductivity; for 800 W/mK and R_{GB} = 1m^{2}K/GW the in-grain thermal conductivity drops by a factor 8, while the cross plane is only reduced by less than a factor 2 (see Figure 32). It is also clear from these curves that not all the values of ($k_{in-grain}$, R_{GB}) which result in an effective in-plane thermal conductivity equal to what was measured are compatible with the measured cross-plane values, and vice versa. Note for instance that while a $k_{in-grain}$ of 800 W/mK may result in an in-plane thermal conductivity of 95 W/mK when R_{GB}=1.05 m^{2}K/GW, it will require a R_{GB} well above 2 m^{2}K/GW for obtaining a cross-plane above 150 W/mK. In fact there is only one set ($k_{in-grain}$, R_{GB}) of values able to simultaneously fulfill both cross-plane and in-plane measurements, resulting in $k_{in-grain}$=250 W/mK and R_{GB}=0.625 m^{2}K/GW respectively (Figure 32, black dotted line). Nevertheless when the experimental error in the measurements is considered, a range of allowed values rather than a single set of values is obtained. This is shown in Figure 32 (blue dotted lines) and allows to estimate the incertitude in ($k_{in-grain}$, R_{GB}), resulting in $150\text{W/mK} < k_{in-grain} < 400\text{W/mK}$ and $0.26\text{m}^2\text{K/GW} < R_{GB} < 1.06\text{m}^2\text{K/GW}$. Hence even if the boundaries were completely clean (R_{GB}=0.06 m^{2}K/GW) the thermal conductivity of this diamond film would not exceed 300 W/mK. Most likely candidates for this reduced thermal conductivity are point defects such as silicon from the substrate and a high density of dislocations. On the other hand the values for R_{GB} are much higher than the ones calculated for a simple lattice mismatch by molecular dynamics, clearly indicating that there is an accumulation of defects in this region increasing the thermal resistance of the grain boundary.

The curves shown in Figure 32 also allow testing the validity of the approach given in Eq. 6 for this material. For this, we fitted Eq. 6 to the results obtained in the 2D slab containing the real grain structure value with d as a single fitting parameter for each $k_{in-grain}$ (see Figure 32, red curves). It is observed that for the in-plane thermal conductivity this simple approach is only valid when the value of R_{GB} is low, and worsens when the lattice conductivity is larger. This is a result of the columnar structure of the diamond film, for which the top half of the film consists of grain boundaries which are in average much further apart than in the bottom half of the film. Thus when the thermal resistance of the boundaries is high enough, the thermal resistance of the bottom part is much higher than in the top part, especially if $k_{in-grain}$ is high, and the heat flux becomes two dimensional instead of one dimensional. This is not captured by a single grain size in Eq. 6, and results in the underestimation of the in-plane thermal conductivity of the film. This behavior is mitigated for the cross-plane thermal conductivity due to the long grains and their more homogenous size distribution in the XY plane, resulting in a much better fit of Eq. 6 to the results obtained when the real grain structure is considered.

The impact of the lattice thermal conductivity and grain boundaries on the commonly reported anisotropy of the thermal conductivity for polycrystalline diamond is summarized in Figure 33. Here this phenomenon naturally emerges from the polycrystalline grain geometry when the thermal resistance of the grain boundaries is considered; the magnitude of the anisotropy

depends on both $k_{in-grain}$ and R_{GB} (see Figure 33a). For a polycrystalline diamond film with very low lattice defects in its near nucleation site, the anisotropy in thermal conductivity is higher than when the quality of the diamond is low. Even if the grain boundaries are defect-free, the thin polycrystalline diamond film shows a non-negligible anisotropy in its thermal conduction which increases linearly with $k_{in-grain}$ (Figure 33b).
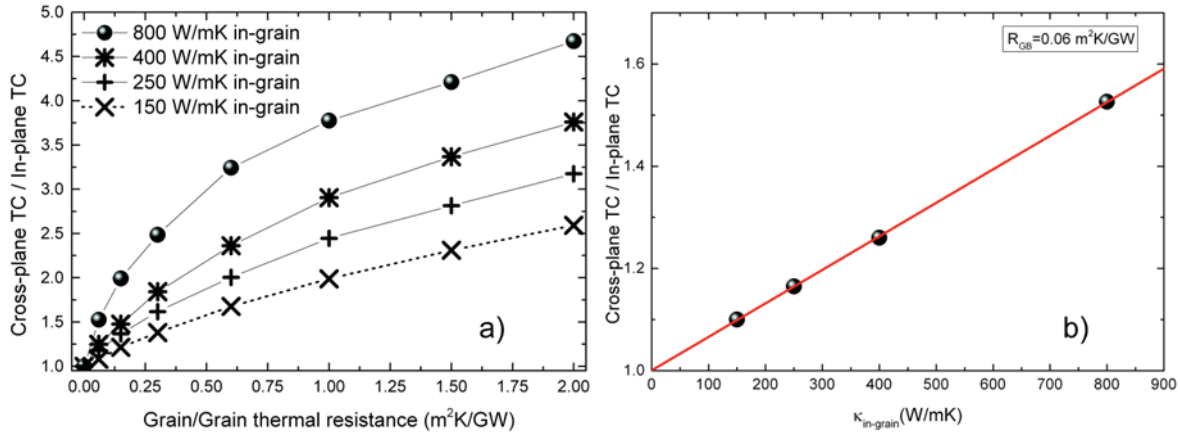

Figure 33: Effective Anisotropy of CVD Diamond Film
(a) Effective anisotropy of the thermal conductivity of the diamond film as a function of the grain boundary thermal resistance for different values of the diamond lattice thermal conductivity. (b) Effective anisotropy as a function of the lattice thermal conductivity for clean grain boundaries.

4.5   Conclusions

The in-plane and cross-plane thermal conductivity of a polycrystalline diamond thin film near its nucleation region was assessed. The grain structure determined by TEM in a long slab of the film was ported to a finite element solver in which the equivalent heat equation corresponding to Raman thermography assisted by TiO_2 nanoparticles and picosecond TDTR thermal measurements performed in the film was solved. With this methodology, we were able to simultaneously quantify the contribution to the thermal resistance of the lattice and grain boundaries in this material. We found that the lattice thermal conductivity of the near nucleation diamond 5-8 times smaller than the one observed in Section 2.1 single crystals diamonds, clearly indicating the presence of defects inside the grains. On the other hand, we found the thermal resistance between grains much higher than the values computed from molecular dynamic for clean boundaries, evidencing that defects are also accumulated in these boundaries. Finally, we have shown that the anisotropy commonly observed in polycrystalline diamond may be easily explained when the real grain structure is included in the thermal model. Besides, we found that it is expected that this anisotropy increases linearly with the lattice thermal conductivity of the films.

5. Major Findings and Contributions

5.1 Viability of TDTR and Raman for the Measurement of Thermal Conductivity in CVD Diamond Thin Films

At the outset of this program, one of the major questions that was posed to our team was to determine the merits of using TDTR and Raman thermometry (Figure 34) for the measurement of the thermal conductivity of thin CVD diamond films which were only recently discussed in the literature prior to the inception of this program. Through rigorous work and collaboration, were able to develop a procedure which enabled repeatable results from TDTR measurements and showed that the underlying microstructure can contribute to the variation in thermal measurements. Thus, either measurements at the same location (very difficult) or a sufficient number of measurements which averaged over the underlying microstructural effects was needed to create repeatable results that also matched well with the Raman measurements for in-plane thermal conductivity. For all of our measurements, the uncertainty averaged around 10-15% for these measurements. Uncertainties that are much lower than this (e.g., 2-5%) are not realistic. It should be noted that in-plane Raman measurements also average over a large number of grains and inherently present an average thermal conductivity coming from the microstructure. We were able to use localized TDTR measurements, however, to demonstrate that we can see the thermal conductivity of individual grains in thick CVD diamond samples and this correlated well with electron backscatter diffraction (EBSD) maps of the microstructures. This was the first time that such measurements were ever made. Finally, we were able to implement ERT measurements to also compare with Raman and TDTR. Overall, the data show that it is possible to make in-plane thermal conductivity measurements using all three methods, with the most effort being placed in the TDTR technique. Second, for vertical thermal conductivity, we found that none of the methods can yield low uncertainty on thin CVD diamond films since it is difficult to generate a temperature drop across the CVD diamond layer that we can adequately measure. TDTR was best for making these measurements and proved that it could measure bulk films up to 2200 W/mK. However, as the thermal conductivity increased, it was found that the error on the measurements increased due to the fact that it became difficult to create a sufficient temperature rise due to the highly thermally conductive material. For comparable measurements, methods such as 3-omega was needed to measure thermal conductivity of highly conductive diamond, but again with very large error bars, on the order of 10-20%. A summary of the merits of each technique is in Table 4.

Figure 34: TDTR and Raman Setup
Image of TDTR (left) and Raman (right) techniques used for thermal conductivity analysis in this program.

5.2 Use of Raman and PL to show Stress Gradients in GaN on Diamond Films showing they are highly stressed at the Interface

A key implementation of CVD diamond films is their integration with GaN to provide sufficient heat spreading near the channel of the HEMT devices. This has been done through the growth of CVD diamond on the backside of GaN buffer layers by groups like NRL and Element 6 or through the bonding of GaN to CVD diamond by groups like BAE systems. While the thermal performance of these systems have shown great promise, there are stresses that exist in the GaN that arise from the CVD diamond growth or attachment process. For layers where the CVD diamond is grown onto the GaN, it was observed that a large tensile stress gradient exists in the GaN layer, being more tensile near the top growth surface and having a smaller tensile stress near the GaN-Diamond growth interface (Figure 35). For CVD diamond that is bonded to the GaN, a much smaller stress is seen, as expected. While not studied in this program, these stress gradients may play an additional role in the reliability and failure of GaN on Diamond HEMTs and must be understood through future investigations.
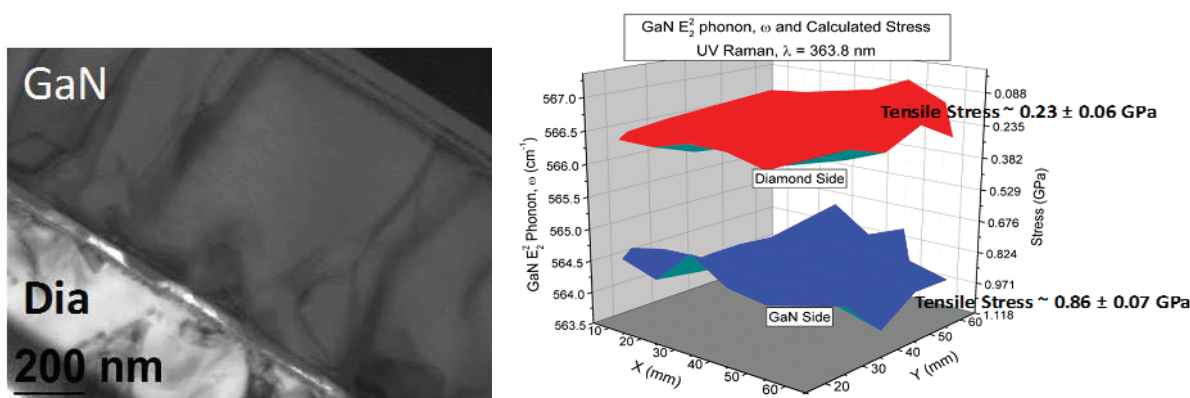

Figure 35: Stress in GaN on Diamond Films
Image showing the interface between CVD diamond grown onto the backside of a GaN buffer layer (left). Corresponding stress on the GaN free surface showing a large tensile stress while the GaN near the diamond interface shows a smaller tensile stress.

5.3 SiN$_x$ Dielectric is Key in the Growth of Diamond on GaN leading to low TBR Interfaces

This work as part of the larger program confirmed that even with its relatively low thermal conductivity, SiN$_x$ is the best choice as a material for helping to facilitate the growth of diamond directly on GaN while also resulting in low TBR as characterized via TDTR. A series of experiments that involved using AlN, SiN$_x$, and no interfacial layer showed that SiN$_x$ was the best amongst the various interfaces used. It was found through HAADF imaging that a mixture of Si, SiC, C, and SiN$_x$ phases exist as shown in Figure 36. When using a thin layer of SiN$_x$ (~5nm) it was found that a smooth transition with intermixing of Si-C-N elements takes place throughout the interface, resulting in the lowest TBR measured to date between GaN and diamond. This result was not expected and shows that a complex chemistry of the interface must be controlled in order to reduce the TBR. For the AlN and no interfacial layers, voids and etching of the GaN occurred which resulted in increases to the TBR. Thus, SiN$_x$ has become the best interface for the growth of CVD diamond on GaN.
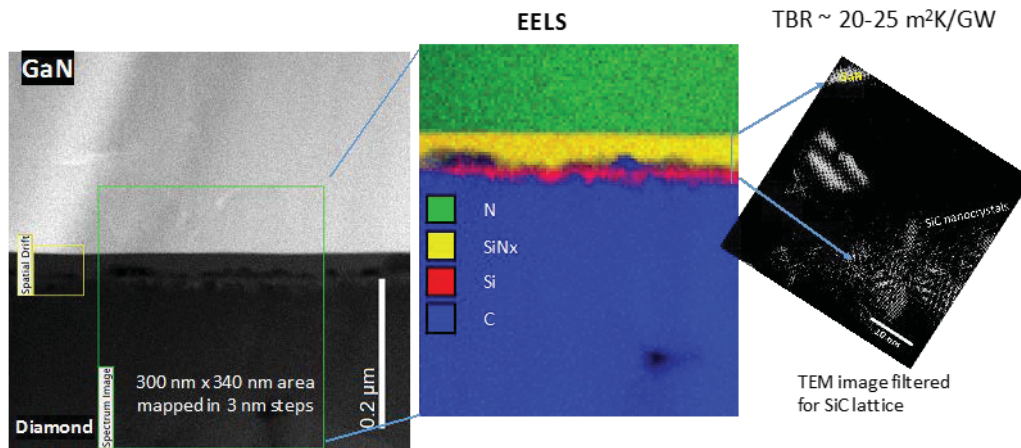
Approved for public release; distribution is unlimited.

Figure 36: Composition of GaN on Diamond Interface
Data showing the image of a GaN-Diamond interface with a silicon nitride layer that has converted to a mixture of Si, C, SiC, and SiN regions.

5.4 Texture Impact to the Thermal Resistance of the CVD Diamond and Patterning the Interfaces may lead to a way to Help Induce Preferred 110 Textures

Methods to decrease the thermal boundary resistance at CVD diamond interfaces were attempted by nanopatterning the surface of the growth substrate, in this case Si. In the work on the measurement of the TBR at patterned interfaces between silicon and CVD diamond, it was observed that the growth of the CVD diamond on these patterned Si structures resulted in preferential (110) texturing of the diamond grains (Figure 37). Improvement in the textural control was seen when reducing the size of the nanopattern height and the spacing to be on the order of 50 and 140 nm, respectively. This (110) texturing produces higher cross-plane thermal conductivities of the CVD diamond films due to the reduction in alternatively oriented crystals and the resistive phonon scattering processes that can result. In addition to the reported impact on the TBR, this method for created highly textured CVD diamond films may provide an avenue for the growth of higher quality (and thus higher thermal conductivity) material by templating the growth from patterned surfaces.
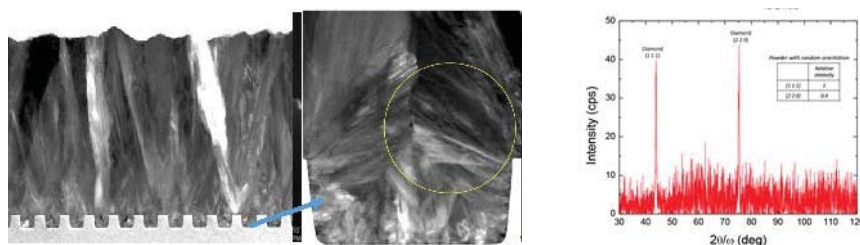

Figure 37: Image of Diamond on Si with Patterned Interfaces
Image showing the patterned Si interface with CVD diamond (left) and XRD measurements of texture (right).

5.5   Use of TEM along with Orientation Mapping provides a True Analysis of the Grain Size Distribution in CVD Diamond Films

A key factor in interpreting the thermal conductivity data was the need to understand the microstructure. The primary factors quantified were grain size, twinning, and texture of the CVD diamond, regardless of the interfacial chemistry. The ability to identify the transition from ultra-nanocrystalline, to nanocrystalline diamond as the growth process progresses, as well as the orientation and sizes of the grains were all important elements of the program towards understanding the thermal properties associated with the structure of the diamond films. In general, SEM analysis has been used to characterize the grain size by looking at plan view images. However, by using orientation imaging analysis, it was shown that a true measurement of the real grain size distribution could be measured which often resulted in an average grain size being a factor of 2 smaller than that measured by SEM plan view images (Figure 38). This method is the first of its kind applied to CVD diamond and helps to provide a new standard for characterizing the microstructure of CVD diamond for input into thermal transport models.
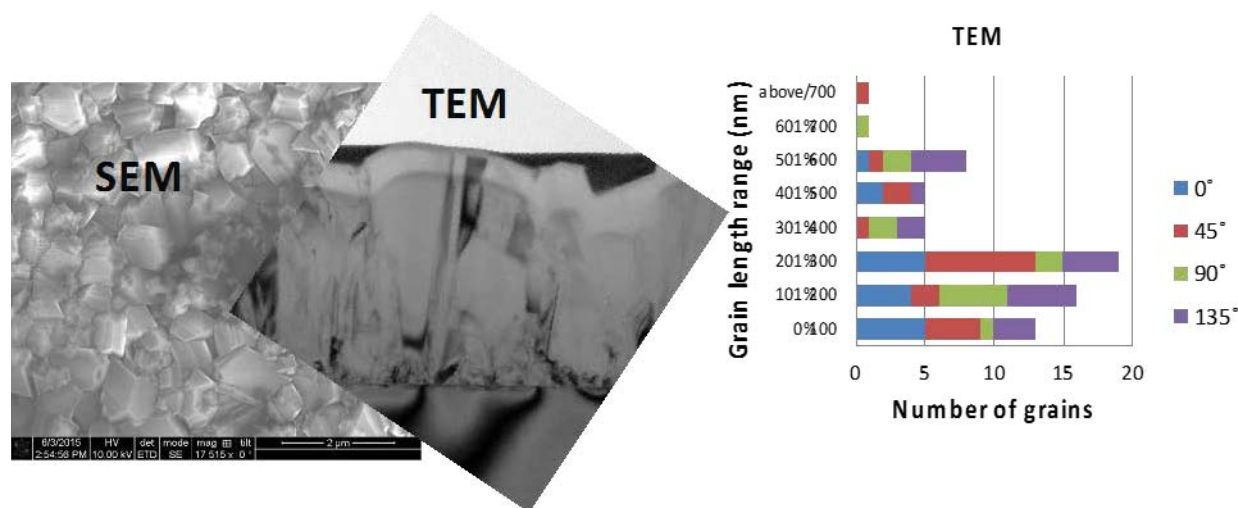

Figure 38: TEM vs SEM Imaging of Grain Size
Images showing the grain structure by plan view SEM, cross section TEM (left) and the resulting grain size distribution from orientation imaging using TEM (right).

5.6   Demonstrated for the First Time the Correlation between Local Thermal Conductivity and Underlying Microstructure

Through the use of the mapping of grain orientation via TEM imaging and orientation imaging analysis along with TDTR mapping, the correlation between the orientation of a given grain and the thermal conductivity within that grain has been demonstrated (Figure 39). Through the use of the fine spatial resolution of TDTR, thermal conductivity maps were generated to determine how the conductivity varies as a function of position within a grain due to effects such as proximity to a nearby grain boundary, as well as due to the orientation of the grain itself. These were the first maps ever taken showing the electron backscattered detection imaging of grains and how the thermal conductivity changes with grain orientation on a size scale of around 1 μm. Data clearly show that thermal conductivity reduces as one approaches the grain boundaries due to the larger number of defects associated with the grain boundaries. By averaging over a

sufficient number of grains, it is possible to reach an average value that is consistent with more macroscopic measurements of CVD diamond thermal conductivity.
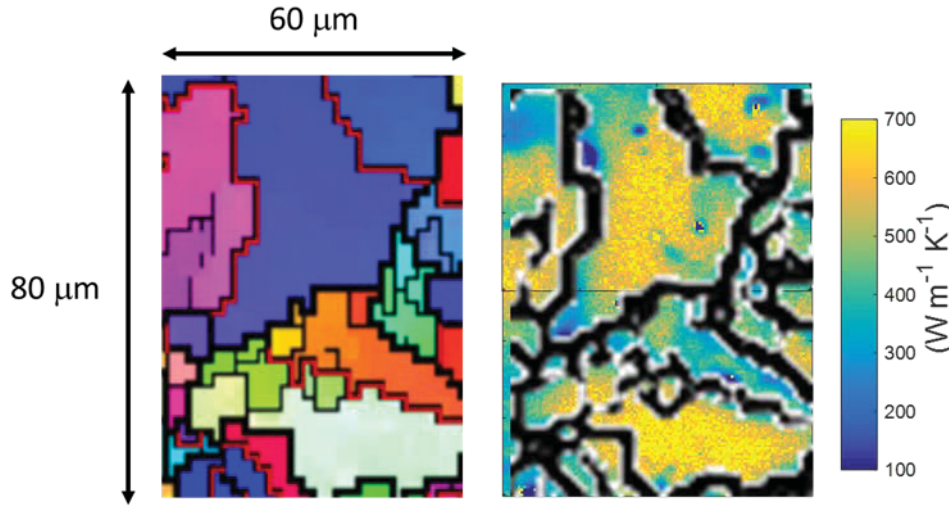

Figure 39: EBSD and TDTR Mapping of Thermal Conductivity and Grain Orientation in CVD Diamond

EBSD orientation imaging of a bulk CVD diamond sample (left) and the mapping of thermal conductivity by TDTR (right) showing the strong correlation between microstructure and the spatial variation in thermal conductivity.

5.7 GaN Bonded to Diamond Demonstrated 25 W/mm DC Power Densities with TBR ~ 17 m^{2}K/GW

The majority of the techniques for integrating CVD diamond with GaN is performed by seeding the growth of diamond on GaN with a SiN$_x$ interfacial layers. However, CVD diamond can also be integrated with GaN by bonding using a low temperature process involving an interfacial layer. This proprietary method was performed by BAE Systems and samples of the GaN on diamond HEMTs were provided to our team for analysis (Figure 40). Analysis of the TBR showed a value of 17 m^{2}K/GW which is lower than many of the CVD diamond samples grown by other suppliers. In addition, we were able to test these samples up to 25 W/mm power densities under DC conditions.
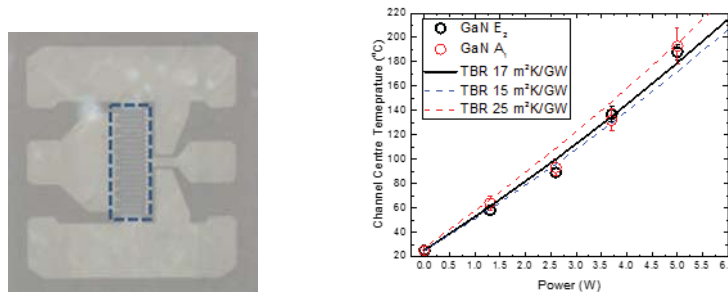

Figure 40: GaN on Diamond HEMTs with Bonded Interfaces

Image showing the GaN on diamond HEMT provided by BAE Systems (left) and the measured device temperature by Raman versus input power (right).

5.8 Use of Diamond Seeds in the Range of 40-50 nm Produced the Best Diamond/Si and Diamond/GaN Interfaces

The growth of CVD diamond onto GaN is depends on the seeding of the surface with diamond nanocrystals (Figure 41). A study of seeding of the diamond with nanocrystals ranging from 4 nm to 00 nm showed that the best interfaces were obtained with diamond seeds in the range of 40-50 nm. This was accomplished by measuring CVD diamond on GaN from two different sources, both showing a similar result. Thus, it has been determined that the optimal seeding size is in the range of 40-50 nm. Additional work is needed to optimize the seed deposition process and seed density.
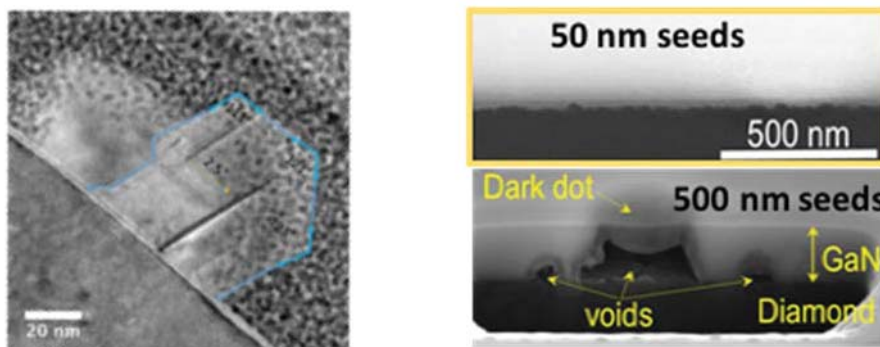

Figure 41: Image of Nucleating Seeds for CVD Diamond Growth
Images showing the interfaces between GaN and Diamond with diamond nanocrystalline seeds. For large seeds, voids were observed at the growth interfaces.

6. References

[1] T.E. Beechem, and J.R. Serrano, "Raman Thermometry of Microdevices: Choosing a Method to Minimize Error". Spectroscopy, 2011. 26(11): p. 36-44.

[2] Y.L. Du, Y. Deng, and M.S. Zhang, "Variable-temperature Raman scattering study on anatase titanium dioxide nanocrystals". Journal of Physics and Chemistry of Solids, 2006. 67(11): p. 2405-2408.

[3] C. Burda, et al., "Enhanced nitrogen doping in TiO2 nanoparticles". Nano Letters, 2003. 3(8): p. 1049-1051.

[4] P. Achatz, et al., "Optical properties of nanocrystalline diamond thin films". Applied Physics Letters, 2006. 88(10).

[5] J. Jimenez, and J.W. Tomm, "Raman Spectroscopy, in Spectroscopic Analysis of Optoelectronic Semiconductors". 2016, Springer International Publishing: Switzerland. p. 77-142.

[6] T.L. Bergman, et al., Fundamentals of Heat and Mass Transfer. Seventh Edition ed. 2011: John Wiley & Sons, Inc.

[7] D. Cabaleiro, et al., "Thermal conductivity of dry anatase and rutile nano-powders and ethylene and propylene glycol-based TiO_2 nanofluids". The Journal of Chemical Thermodynamics, 2015. 83: p. 67-76.

[8] T.L. Bougher, et al. "Experimental considerations of CVD diamond film measurements using time domain thermoreflectance". in Thermal and Thermomechanical Phenomena in Electronic Systems (ITherm), 2017 16th IEEE Intersociety Conference on. 2017. IEEE.

[9] G. Pavlidis, et al., "Characterization of AlGaN/GaN HEMTs Using Gate Resistance Thermometry". IEEE Transactions on Electron Devices, 2017. 64(1): p. 78-83.

[10] T.L. Bougher, et al., "Thermal Boundary Resistance in GaN Films Measured by Time Domain Thermoreflectance with Robust Monte Carlo Uncertainty Estimation". Nanoscale and Microscale Thermophysical Engineering, 2016. 20(1): p. 22-32.

[11] C.E. Papadopoulos, and H. Yeung, "Uncertainty estimation and Monte Carlo simulation method". Flow Measurement and Instrumentation, 2001. 12(4): p. 291-298.

[12] D. G. Cahill, "Analysis of heat flow in layered structures for time-domain thermoreflectance," Review of Scientific Instruments, vol. 75, pp. 5119-5122, Dec 2004.

[13] A. J. Schmidt, X. Y. Chen, and G. Chen, "Pulse accumulation, radial heat conduction, and anisotropic thermal conductivity in pump-probe transient thermoreflectance," Review of Scientific Instruments, vol. 79, Nov 2008.

[14] Y. X. Wang, J. Y. Park, Y. K. Koh, and D. G. Cahill, "Thermoreflectance of metal transducers for time-domain thermoreflectance," Journal of Applied Physics, vol. 108, Aug 15 2010.

[15] G. T. Hohensee, W. P. Hsieh, M. D. Losego, and D. G. Cahill, "Interpreting picosecond acoustics in the case of low interface stiffness," Review of Scientific Instruments, vol. 83, Nov 2012.

[16] A. Sood, J. Cho, K. D. Hobart, T. I. Feygelson, B. B. Pate, M. Asheghi, et al., "Anisotropic and inhomogeneous thermal conduction in suspended thin-film polycrystalline diamond," Journal of Applied Physics, vol. 119, p. 175103, 2016.

[17] E. H. Buyco and F. E. Davis, "Specific heat of aluminum from zero to its melting temperature and beyond. Equation for representation of the specific heat of solids," Journal of Chemical and engineering data, vol. 15, pp. 518-523, 1970.

[18]   A. C. Victor, "Heat capacity of diamond at high temperatures," The Journal of Chemical Physics, vol. 36, pp. 1903-1911, 1962.

[19]   C. D. Wei, X. Zheng, D. G. Cahill, and J. C. Zhao, "Invited Article: Micron resolution spatially resolved measurement of heat capacity using dual-frequency time-domain thermoreflectance," Review of Scientific Instruments, vol. 84, Jul 2013.

[20]   F. Faili, W. Huang, J. Calvo, M. Kuball, and D. Twitchen, "Disturbed and scattered: The Path of thermal conduction through diamond lattice," in Thermal and Thermomechanical Phenomena in Electronic Systems (ITherm), 2016 15th IEEE Intersociety Conference on, 2016, pp. 1133-1138.

[21]   D. Altman, M. Tyhach, J. McClymonds, S. Kim, S. Graham, J. Cho, et al., "Analysis and characterization of thermal transport in GaN HEMTs on Diamond substrates," in Thermal and Thermomechanical Phenomena in Electronic Systems (ITherm), 2014 IEEE Intersociety Conference on, 2014, pp. 1199-1205.

[22]   A. J. Schmidt, "Optical characterization of thermal transport from the nanoscale to the macroscale," Massachusetts Institute of Technology, 2008.

[23]   J. Liu, J. Zhu, M. Tian, X. Gu, A. Schmidt, and R. Yang, "Simultaneous measurement of thermal conductivity and heat capacity of bulk and thin film materials using frequency-dependent transient thermoreflectance method," Review of Scientific Instruments, vol. 84, p. 034902, 2013.

[24]   T. L. Bougher, L. Yates, C.-F. Lo, W. Johnson, S. Graham, and B. A. Cola, "Thermal boundary resistance in GaN films measured by time domain thermoreflectance with robust Monte Carlo uncertainty estimation," Nanoscale and Microscale Thermophysical Engineering, vol. 20, pp. 22-32, 2016.

[25]   C. L. X. Gu, J. Xie, E. Beam, M. Becker, T. A. Grotjohn, J. Anaya, and M. Kuball, "GaN-on-Diamond with Ultra-Low Thermal Barrier Resistance," presented at the GOMACTech, Orlando, FL, 2016.

[26]   J. W. Pomeroy, R. B. Simon, H. Sun, D. Francis, F. Faili, D. J. Twitchen, et al., "Contactless thermal boundary resistance measurement of GaN-on-diamond wafers," IEEE Electron Device Letters, vol. 35, pp. 1007-1009, 2014.

[27]   Y. Zhou, J. Anaya, J. Pomeroy, H. Sun, X. Gu, A. Xie, et al., "Barrier Layer Optimization for Enhanced GaN-on-diamond Device Cooling," ACS Applied Materials & Interfaces, 2017.

[28]   H. Siegle, G. Kaczmarczyk, L. Filippidis, A. Litvinchuk, A. Hoffmann, and C. Thomsen, "Zone-boundary phonons in hexagonal and cubic GaN," Physical Review B, vol. 55, p. 7000, 1997.

[29]   J. Anaya, S. Rossi, M. Alomari, E. Kohn, L. Tóth, B. Pécz, et al., "Control of the in-plane thermal conductivity of ultra-thin nanocrystalline diamond films through the grain and grain boundary properties," Acta Materialia, vol. 103, pp. 141-152, 2016.

[30]   Y.-H. Yeh, K.-M. Chen, Y.-H. Wu, Y.-C. Hsu, T.-Y. Yu, and W.-I. Lee, "Hydrogen etching of GaN and its application to produce free-standing GaN thick films," Journal of Crystal Growth, vol. 333, pp. 16-19, 2011.

[31]   F. D. L. P. e. al., "Hyperspy/Hyperspy:Hyperspy1.3," Jan. 2017.

[32]   R. F. Egerton, Electron energy-loss spectroscopy in the electron microscope: Springer Science & Business Media, 2011.

[33]   M. Alam, M. P. Manoharan, M. A. Haque, C. Muratore, and A. Voevodin, "Influence of strain on thermal conductivity of silicon nitride thin films," Journal of Micromechanics and Microengineering, vol. 22, p. 045001, 2012.

List of Abbreviations, Acronyms, and Symbols

ACRONYM	DESCRIPTION
AlN	Aluminum Nitride
CVD	Chemical Vapor Deposition
DARPA	Defense Advanced Research Projects Agency
EBSD	Electron Backscatter Diffraction
EELS	Electron Energy Loss Spectroscopy
EOM	electro-optic modulator
ERT	Electrical Resistance Thermometry
FEA	Finite Element Analysis
FEM	Finite Element Model
FIB	Focused Ion Beam
FWHM	Full Width at Half Maximum
GaN	Gallium Nitride
GT	Georgia Tech
HAADF	High Angle Annular Dark Field
HEMT	High Electron Mobility Transistor
ICP	Inductively Coupled Plasma
IPA	Isopropyl Alcohol
ITC	International Technology Center
LED	Light Emitting Diode
LO	Longitudinal Optical
MC	Monte Carlo
MFP	Mean Free Path
MPCVD	Microwave Plasma-Assisted Chemical Vapor Deposition
NCD	Nanocrystalline Diamond
NJTT	Near Junction Thermal Transport
NRL	Naval Research Laboratory
PECVD	Plasma-Enhanced Chemical Vapor Deposition
PED	Precession Electron Diffraction
RIE	Reactive Ion Etch
RTD	Resistance Temperature Device
SAED	Selective Area Electron Diffraction
SEM	Scanning Electron Microscopy
Si	Silicon
SiC	Silicon Carbide
SiN	Silicon Nitride (non-stoichiometric)
STEM	Scanning Transmission Electron Microscope
TBR	Thermal Boundary Resistance
TC	Thermocouple
TDTR	Time Domain Thermal Reflectance
TEM	Transmission Electron Microscopy
UV	Ultraviolet
XRD	X-ray Diffraction

SYMBOL	DESCRIPTION
A_R	Electrical Resistance Calibration Coefficient
A_ω	Raman Calibration Coefficient
C_{dia}	Heat Capacity of Diamond
C_p	Specific Heat
d	Average Grain Size
δk	Measurement Uncertainty for Thermal Conductivity
δy	Uncertainty in derived quantity y
df/dx_i	Sensitivity coefficient for function f wrt parameter x_i
$G_{RTD/NCD}$	Thermal conductance between RTD and NCD film
$G_{NCD/AL}$	Thermal conductance between NCD and AL films
$G_{NCD/Si}$	Thermal conductance between Si and NCD films
$k_{in\text{-}plane}$	In plane thermal conductivity
k_{Al}	Thermal Conductivity of Aluminum
k_{dia}	Thermal conductivity of diamond
k_{eff}	Effective Thermal Conductivity
k_{ERT}	Thermal Conductivity Measured by Electrical Resistance Thermometry
k_{raman}	Thermal Conductivity Measured by Raman Spectroscopy
p_i	ith particle for temperature measurement
ρ	Density
R	Electrical Resistance
R_{GB}	Resistance at grain boundaries
R_o	Reference Electrical Resistance
$S_{p,avg}$	Average sensitivity of a TDTR measurement
T	Temperature
T_o	Temperature Reference
T_{exp}	Experimental Temperature Measurement
t_{AL}	Thickness of Aluminum
t_{NCD}	Thickness of Nanocrystalline Diamond
ΔT	Change in temperature
ω	Raman Peak Shift
ω_o	Raman Peak Reference
y	Derived Quantity